

Reduced operator inference for nonlinear partial differential equations

Elizabeth Qian*

Ionuț-Gabriel Farcaș†

Karen Willcox†

February 28, 2022

Abstract

We present a new scientific machine learning method that learns from data a computationally inexpensive surrogate model for predicting the evolution of a system governed by a time-dependent nonlinear partial differential equation (PDE), an enabling technology for many computational algorithms used in engineering settings. Our formulation generalizes to the function space PDE setting the Operator Inference method previously developed in [B. Peherstorfer and K. Willcox, *Data-driven operator inference for non-intrusive projection-based model reduction*, Computer Methods in Applied Mechanics and Engineering, 306 (2016)] for systems governed by ordinary differential equations. The method brings together two main elements. First, ideas from projection-based model reduction are used to explicitly parametrize the learned model by low-dimensional polynomial operators which reflect the known form of the governing PDE. Second, supervised machine learning tools are used to infer from data the reduced operators of this physics-informed parametrization. For systems whose governing PDEs contain more general (non-polynomial) nonlinearities, the learned model performance can be improved through the use of *lifting* variable transformations, which expose polynomial structure in the PDE. The proposed method is demonstrated on two examples: a heat equation model problem that demonstrates the benefits of the function space formulation in terms of consistency with the underlying continuous truth, and a three-dimensional combustion simulation with over 18 million degrees of freedom, for which the learned reduced models achieve accurate predictions with a dimension reduction of five orders of magnitude and model runtime reduction of up to nine orders of magnitude.

1 Introduction

Systems governed by nonlinear PDEs are ubiquitous in engineering and scientific application and traditional numerical solvers based on high-dimensional spatial discretizations are computationally expensive even on powerful supercomputers. The development of efficient reduced models for PDEs is therefore an enabling technology for many-query applications such as optimization or uncertainty quantification. Empirical successes in using machine learning to learn complex nonlinear functions from data have motivated many works which use machine learning tools to learn models for scientific problems governed by PDEs. The model learning task in such settings is to learn a map that describes the state evolution within the infinite-dimensional function space in which the spatially continuous PDE state lies. In this work, we consider specifically the task of learning a map that describes the state evolution within a low-dimensional subspace of the underlying infinite dimensional function space, in an approach that combines elements from supervised learning and model reduction. Our method, *Operator Inference for PDEs*, generalizes to the Hilbert space setting the method [42] previously developed in Euclidean space which learns a reduced model that reflects the structure of the system governing equations by drawing on ideas from projection-based model reduction.

In projection-based model reduction, a low-dimensional reduced model for the evolution of a nonlinear PDE is derived by projecting the PDE operators onto a low-dimensional subspace of the underlying infinite-dimensional Hilbert space. Several approaches to defining this approximation subspace have been proposed

*Department of Computing + Mathematical Sciences, California Institute of Technology, Pasadena, CA (eqian@caltech.edu, <http://www.elizabethqian.com>).

†Oden Institute for Computational Engineering and Sciences, University of Texas at Austin, Austin, TX (ionut.farcas@austin.utexas.edu, kwillcox@oden.utexas.edu, <https://kiwi.odn.utexas.edu>).

(see [7] for a review), but a common empirical choice is the proper orthogonal decomposition (POD) subspace, which spans the leading principal components of an available set of state data [8, 34, 49]. For PDEs with only linear and polynomial terms, the projection-based reduced model admits an efficient low-dimensional numerical representation that can be cheaply evaluated at a cost independent of the dimension of the original model [6, 7, 9, 15, 21]. For PDEs with more general nonlinear terms, an additional level of approximation, e.g., interpolation [2, 5, 10, 12, 13, 16, 40], is generally needed to achieve computational efficiency. Alternatively, the works in [6, 15, 27, 28] transform PDEs with general nonlinear terms to representations with only quadratic nonlinearities via the use of structure-exposing *lifting* transformations, and then project the quadratic operators of the resultant lifted PDE to obtain a reduced model.

Traditionally, projection-based model reduction is *intrusive*, because numerical implementation of the reduced models requires access to codes that implement the PDE operators. This is a limitation in settings where the code is inaccessible (e.g., legacy or commercial codes). Methods for *non-intrusive* reduced modeling use data to learn reduced operators: one approach is to learn a map from an input (such as a parameter or initial condition) to the coefficients of the PDE state in a reduced basis. This mapping can be parametrized by radial basis functions [3], a neural network [35, 51, 55] or a nearest-neighbors regression [51]. However, these works do not incorporate knowledge of the system governing equations into the learning parametrizations. The Operator Inference method proposed in [42] draws on projection-based model reduction to use knowledge of a system’s governing ODEs to explicitly learn the projection-based reduced operators for ODE systems containing low-order polynomial nonlinear terms. The incorporation of knowledge of the governing equations allows Operator Inference to provably recover the true intrusive reduced polynomial operators of the governing ODEs under certain conditions [42, 41]. The work in [46] presents the *Lift & Learn* method, which applies Operator Inference method to more general nonlinear ODEs by applying quadratic lifting transformations to ODE state data and then fitting reduced linear and quadratic operators to the lifted data. In a different approach, the work in [32] learns sparse reduced models using sparse regression.

While the aforementioned methods for model reduction are frequently applied to scientific models for systems governed by PDEs, the methods are most often developed for the ODE setting corresponding to models arising from spatial discretization of the PDEs. In this work, we formulate the Operator Inference learning approach in the spatially continuous function space setting for the first time. The function space formulation has the following advantages over the Euclidean formulation: (i) The function space formulation is mesh-independent and consistent with the underlying infinite-dimensional system: e.g., it yields implementations that use inner products that approximate the underlying infinite-dimensional inner product, whereas the ODE formulation using the Euclidean inner product may yield approximations that are inconsistent with the underlying infinite-dimensional system. (ii) The function space formulation allows the Lift & Learn approach to take advantage of more general (in particular, nonlocal) structure-exposing lifting transformations between function spaces, compared to previous work in the ODE setting [46] that considered only pointwise transformations. (iii) The function space setting enables rigorous analysis of error with respect to the underlying function space truth: for example, the reduced-basis community has an extensive literature on function space error estimates for intrusive reduced models [17, 19, 47, 54, 53].

We emphasize that Operator Inference is not intended to replace intrusive model reduction approaches when intrusive approaches are feasible: rather, Operator Inference provides a path to obtaining a reduced model when intrusive approaches such as POD-Galerkin are not feasible. The new function space formulation of Operator Inference that we present here makes clear that non-intrusive reduced modeling approaches can and should be viewed in the context of recent works in supervised learning between function spaces. For example, the work in [39] formulates a random feature model for approximating input-output maps on function spaces. Another approach [33] simultaneously trains two neural networks, one which learns basis functions in which to approximate a solution function, and another which learns the coefficients of the learned basis functions. However, these architectures treat the data as arising from a black box, and do not incorporate structure in system governing equations into their learning architectures. The works in [1, 31] use knowledge of kernel operator structure to inspire a novel neural network architecture for approximating maps between function spaces for PDEs. In this work, we use knowledge of the system governing equations to explicitly parametrize the PDE evolution map by low-dimensional operators which reflect the structure of the PDE, inspired by work in projection-based model reduction.

Our emphasis on learning polynomial operators for possibly transformed system states bears similarities to approaches that seek to learn the linear Koopman operator for observables of nonlinear dynamical systems.

Koopman operator theory states that every nonlinear dynamical system can be exactly described by an infinite-dimensional linear operator that acts on scalar observables of the system [26, 38, 37, 29]. DMD learns a finite-dimensional approximation of the Koopman operator in a given set of observables using a least-squares minimization [56, 48]. The success of this approach is dependent on whether the chosen set of observables defines a space that is invariant or close to invariant with respect to the Koopman operator. Previous works have used dictionary-learning [30], neural networks [52], and kernel methods [25] to define the space of observables. Another recent approach uses neural networks to define coordinates in which terms of a governing equation are identified from a large dictionary of possible terms using sparse regression [11]. In contrast, we propose a physics-informed approach which chooses learning variables based on the known governing PDE.

The remainder of the paper is organized as follows. Section 2 formulates the prediction problem for a system governed by a nonlinear PDE and provides background on POD-Galerkin model reduction. Section 3 presents our Operator Inference formulation for learning mappings between Hilbert spaces which approximate the dynamics of a nonlinear PDE. Section 4 introduces Lift & Learn in the PDE setting, which uses variable transformations to apply Operator Inference to learn quadratic models for non-quadratic PDEs. Section 5 presents numerical results for two examples: (i) a heat equation example which demonstrates that the ODE formulation can lead to results that are inconsistent with the underlying truth, and (ii) a three-dimensional rocket combustion simulation with over 18 million degrees of freedom that takes 45,000 CPU hours to run, which demonstrates the potential of the model learning approach to yield computational gains for high-dimensional engineering simulations. Conclusions are discussed in Section 6.

2 Setting and technical foundations

This section introduces the initial/boundary-value problem for which we seek a reduced model (Section 2.1) and presents the POD-Galerkin approach to model reduction (Section 2.2) on which our method builds.

2.1 Problem formulation

Let Ω be a bounded physical domain in \mathbb{R}^d with Lipschitz continuous boundary $\partial\Omega$, and let $[0, T_{\text{final}}] \subset \mathbb{R}$ be a time interval of interest. Let $s : \Omega \times [0, T_{\text{final}}] \rightarrow \mathbb{R}^d$ denote the d -dimensional physical state. We denote by $s_j : \Omega \times [0, T_{\text{final}}] \rightarrow \mathbb{R}$ the j -th element of the state s , so that

$$s(x, t) = \begin{pmatrix} s_1(x, t) \\ s_2(x, t) \\ \vdots \\ s_d(x, t) \end{pmatrix}. \quad (1)$$

For $j = 1, 2, \dots, d$, let \mathcal{X}_j be a separable Hilbert space of real-valued functions of Ω . We denote by $\mathcal{X} = \mathcal{X}_1 \times \mathcal{X}_2 \times \dots \times \mathcal{X}_d$ the product of the spaces \mathcal{X}_j and endow \mathcal{X} with the natural definition of inner product:

$$\langle s, s' \rangle_{\mathcal{X}} = \sum_{j=1}^d \langle s_j, s'_j \rangle_{\mathcal{X}_j}. \quad (2)$$

Let $f : \mathcal{X} \rightarrow \mathcal{X}$ denote a smooth nonlinear mapping between function spaces. We then consider the (strong form of the) following partial differential equation, written as an ordinary differential equation in the Hilbert space \mathcal{X} :

$$\frac{\partial s}{\partial t} = f(s), \quad s(\cdot, 0) = s_{\text{init}}. \quad (3)$$

We remark that in our numerical examples in Section 5, the \mathcal{X} -inner product is the $L^2(\Omega)$ -inner product; however, our formulation is not restricted to this choice. In what follows, we therefore use $\langle \cdot, \cdot \rangle_{\mathcal{X}}$ to denote an abstract choice of inner product for the Hilbert space \mathcal{X} .

2.2 POD-Galerkin model reduction

The POD-Galerkin approach to model reduction defines a reduced model for an initial/boundary value problem by projecting the operators of the governing PDE onto a low-dimensional subspace spanned by the leading modes of a proper orthogonal decomposition of an available set of state data. Let $s^{(1)}, s^{(2)}, \dots, s^{(K)} \in \mathcal{X}$ denote a set of K snapshots of the solution to eq. (3), taken at different times (and more generally, possibly from multiple trajectories corresponding to e.g., varying initial conditions). The POD subspace of dimension r , denoted \mathcal{X}_r , is the rank- r subspace of \mathcal{X} that minimizes the mean square error between the snapshots and their projections onto \mathcal{X}_r . Let $\mathcal{C} : \mathcal{X} \rightarrow \mathcal{X}$ denote the empirical covariance operator of the snapshots, defined as

$$\mathcal{C}\psi = \sum_{k=1}^K \langle \psi, s^{(k)} \rangle_{\mathcal{X}} s^{(k)}, \quad \psi \in \mathcal{X}. \quad (4)$$

Because \mathcal{C} is compact, non-negative, and self-adjoint on \mathcal{X} , there exists a sequence of eigenvalues λ_i and an associated complete orthonormal basis $\psi_i \in \mathcal{X}$ satisfying $\mathcal{C}\psi_i = \lambda_i \psi_i$, with $\lambda_i \rightarrow 0$ as $i \rightarrow \infty$. The leading r eigenfunctions $\{\psi_i\}_{i=1}^r$ are a POD basis of rank r . That is, $\{\psi_i\}_{i=1}^r$ satisfy $\langle \psi_i, \psi_j \rangle_{\mathcal{X}} = \delta_{ij}$, and are a solution to

$$\min_{\{\psi_i\}_{i=1}^r \in \mathcal{X}} \sum_{k=1}^K \left\| s^{(k)} - \sum_{l=1}^r \langle s^{(k)}, \psi_l \rangle_{\mathcal{X}} \psi_l \right\|_{\mathcal{X}}^2, \quad (5)$$

with attained minimum sum-of-squares objective value $\sum_{i=r+1}^K \lambda_i$.

The POD-Galerkin approximation to eq. (3) approximates the state, $s(x, t)$, in the span of the POD basis as follows:

$$s_{\text{pod}}(x, t) = \sum_{i=1}^r \hat{s}_i(t) \psi_i(x), \quad (6)$$

and evolves the POD state $s_{\text{pod}}(x, t)$ within the POD subspace \mathcal{X}_r by enforcing Galerkin orthogonality of the PDE residual to each function in the POD basis:

$$\left\langle \frac{\partial s_{\text{pod}}}{\partial t}, \psi_l \right\rangle_{\mathcal{X}} = \langle f(s_{\text{pod}}), \psi_l \rangle_{\mathcal{X}}, \quad l = 1, 2, \dots, r. \quad (7)$$

Substituting eq. (6) into eq. (7) yields the following system of r ordinary differential equations (ODEs) for the evolution of $\hat{s}_1(t), \hat{s}_2(t), \dots, \hat{s}_r(t)$, the coefficients of the POD basis functions:

$$\frac{d\hat{s}_l}{dt} = \left\langle f \left(\sum_{i=1}^r \hat{s}_i(t) \psi_i(x) \right), \psi_l(x) \right\rangle_{\mathcal{X}}, \quad (8a)$$

$$\hat{s}_l(0) = \langle s_{\text{init}}(x), \psi_l(x) \rangle_{\mathcal{X}}, \quad (8b)$$

for $l = 1, 2, \dots, r$. The initial-value problem in eq. (8) is referred to as the *reduced model*. However, evaluating the r -dimensional projected dynamics in eq. (8a) requires evaluation of the map f in the infinite-dimensional Hilbert space \mathcal{X} before projecting back down to \mathcal{X}_r .

In the special case where f contains only polynomial nonlinearities, the ODEs which govern the evolution of the POD coefficients eq. (8a) have structure that allows rapid online solution of eq. (8). For example, suppose $f(s) = a(s) + h(s, s)$, where $a : \mathcal{X} \rightarrow \mathcal{X}$ is linear and $h : \mathcal{X} \times \mathcal{X} \rightarrow \mathcal{X}$ bilinear. We note that this definition allows $h(s, s)$ to represent quadratic terms such as s^2 or $s \frac{\partial s}{\partial x}$. Then, eq. (8a) takes the form

$$\frac{d\hat{s}_l}{dt} = \sum_{i=1}^r \hat{s}_i(t) \langle a(\psi_i(x)), \psi_l(x) \rangle_{\mathcal{X}} + \sum_{i,j=1}^r \hat{s}_i(t) \hat{s}_j(t) \langle h(\psi_i(x), \psi_j(x)), \psi_l(x) \rangle_{\mathcal{X}}. \quad (9)$$

If we define the reduced state $\hat{s}(t) \in \mathbb{R}^r$ by $\hat{s}(t) = (\hat{s}_1(t) \quad \hat{s}_2(t) \quad \dots \quad \hat{s}_r(t))^{\top}$, then eq. (9) can be equivalently expressed as

$$\frac{d\hat{s}}{dt} = \hat{A}\hat{s} + \hat{H}(\hat{s} \otimes \hat{s}), \quad (10)$$

where \otimes denotes the Kronecker product, and $\hat{A} \in \mathbb{R}^{r \times r}$ and $\hat{H} \in \mathbb{R}^{r \times r^2}$ are reduced linear and quadratic operators. Denote by $\hat{a}_{l,i}$ the i -th entry of the l -th row of \hat{A} and denote by $\hat{h}_{l,ij}$ the $((i-1)r+j)$ -th entry of the l -th row of \hat{H} . Then, the entries of \hat{A} and \hat{H} are given by $\hat{a}_{l,i} = \langle \psi_l, a(\psi_i) \rangle_{\mathcal{X}}$, and $\hat{h}_{l,ij} = \langle \psi_l, h(\psi_i, \psi_j) \rangle_{\mathcal{X}}$, for $l, i, j = 1, 2, \dots, r$. Computing the reduced operators \hat{A} and \hat{H} is considered *intrusive* because it requires access to the PDE operators a and h . We propose a *non-intrusive* method for learning the reduced operators from data in Section 3.

3 Operator Inference for PDEs

This section presents our formulation of the Operator Inference method for learning reduced models for nonlinear PDEs. Section 3.1 introduces the learning formulation as a linear least-squares problem. Section 3.2 discusses numerical properties of the method.

3.1 Formulation

Operator Inference *non-intrusively* learns a reduced model for eq. (3) from state snapshot and time derivative data. That is, suppose that for each state snapshot $s^{(k)}$, for $k = 1, 2, \dots, K$, the corresponding time derivative $\dot{s}^{(k)} = f(s^{(k)})$ is available. We will approximate the PDE state in \mathcal{X}_r , the POD subspace of rank r :

$$s_{\text{opinf}}(x, t) = \sum_{i=1}^r \tilde{s}_i(t) \psi_i(x), \quad (11)$$

where the basis functions ψ_i are defined as in Section 2.2. Then, informed by the form of the POD-Galerkin reduced model, we fit to the available data a model for the evolution of s_{opinf} within \mathcal{X}_r with the following form:

$$\frac{\partial s_{\text{opinf}}}{\partial t} = f_r(s_{\text{opinf}}(x, t); \tilde{a}_{l,i}, \tilde{h}_{l,ij}) \quad (12)$$

where $f_r(\cdot; \tilde{a}_{l,i}, \tilde{h}_{l,ij}) : \mathcal{X}_r \rightarrow \mathcal{X}_r$ has the explicit polynomial form

$$f_r(s_{\text{opinf}}(x, t); \tilde{a}_{l,i}, \tilde{h}_{l,ij}) = \sum_{l=1}^r \left(\sum_{i=1}^r \tilde{a}_{l,i} \tilde{s}_i(t) + \sum_{i,j=1}^r \tilde{h}_{l,ij} \tilde{s}_i(t) \tilde{s}_j(t) \right) \psi_l(x), \quad (13)$$

where $\tilde{s}_i(t) = \langle \psi_i(x), s_{\text{opinf}}(x, t) \rangle$. To learn the parameters $\tilde{a}_{l,i}$ and $\tilde{h}_{l,ij}$, the snapshot and time derivative data are projected onto the POD subspace \mathcal{X}_r as follows:

$$s_{\text{proj}}^{(k)} = \sum_{l=1}^r \langle s^{(k)}, \psi_l \rangle_{\mathcal{X}} \psi_l, \quad \dot{s}_{\text{proj}}^{(k)} = \sum_{l=1}^r \langle \dot{s}^{(k)}, \psi_l \rangle_{\mathcal{X}} \psi_l. \quad (14)$$

The parameters $\tilde{a}_{l,i}$ and $\tilde{h}_{l,ij}$, for $l, i, j = 1, 2, \dots, r$, are fit by minimizing the following least-squares objective:

$$\min_{\tilde{a}_{l,i} \in \mathbb{R}, \tilde{h}_{l,ij} \in \mathbb{R}} \frac{1}{K} \sum_{k=1}^K \left\| f_r(s_{\text{proj}}^{(k)}; \tilde{a}_{l,i}, \tilde{h}_{l,ij}) - \dot{s}_{\text{proj}}^{(k)} \right\|_{\mathcal{X}}^2. \quad (15)$$

Since \mathcal{X}_r is isomorphic to \mathbb{R}^r , we can collect the POD coefficients of the state and time derivative data as follows:

$$\tilde{s}^{(k)} = \begin{pmatrix} \langle s^{(k)}, \psi_1 \rangle_{\mathcal{X}} \\ \langle s^{(k)}, \psi_2 \rangle_{\mathcal{X}} \\ \vdots \\ \langle s^{(k)}, \psi_r \rangle_{\mathcal{X}} \end{pmatrix}, \quad \dot{\tilde{s}}^{(k)} = \begin{pmatrix} \langle \dot{s}^{(k)}, \psi_1 \rangle_{\mathcal{X}} \\ \langle \dot{s}^{(k)}, \psi_2 \rangle_{\mathcal{X}} \\ \vdots \\ \langle \dot{s}^{(k)}, \psi_r \rangle_{\mathcal{X}} \end{pmatrix}, \quad (16)$$

for $k = 1, 2, \dots, K$. Then, eq. (15) can be equivalently expressed as

$$\arg \min_{\tilde{A} \in \mathbb{R}^{r \times r}, \tilde{H} \in \mathbb{R}^{r \times r^2}} \frac{1}{K} \sum_{k=1}^K \left\| \tilde{A} \tilde{s}^{(k)} + \tilde{H} (\tilde{s}^{(k)} \otimes \tilde{s}^{(k)}) - \dot{\tilde{s}}^{(k)} \right\|_{\mathbb{R}^r}^2, \quad (17)$$

where $\tilde{a}_{l,i}$ is the i -th entry of the l -th row of \tilde{A} and $\tilde{h}_{l,ij}$ is the $((i-1)r+j)$ -th entry of the l -th row of \tilde{H} . The inferred matrix operators \tilde{A} and \tilde{H} define a reduced model of the form

$$\frac{\partial \tilde{s}}{\partial t} = \tilde{A} \tilde{s} + \tilde{H} (\tilde{s} \otimes \tilde{s}). \quad (18)$$

Due to the inherent symmetry in the quadratic terms $\tilde{h}_{l,ij} \tilde{s}_i(t) \tilde{s}_j(t)$ and $\tilde{h}_{l,ji} \tilde{s}_j(t) \tilde{s}_i(t)$ in eq. (13) the solution to eq. (15) (and therefore to eq. (17)) is not unique. We therefore specify that we seek the solution to eq. (15) (equivalently, to eq. (17)) that minimizes the sum of the operator Frobenius norms:

$$\left\| \tilde{A} \right\|_F^2 + \left\| \tilde{H} \right\|_F^2 = \sum_{l,i,j=1}^r \left| \tilde{h}_{l,ij} \right|^2 + \sum_{l,i=1}^r |\tilde{a}_{l,i}|^2. \quad (19)$$

The solution to eq. (15)/eq. (17) that minimizes eq. (19) will yield a *symmetric* quadratic operator \tilde{H} in the sense that $\tilde{h}_{l,ij} = \tilde{h}_{l,ji}$.

3.2 Numerical considerations

The formulation of Operator Inference as a linear least-squares problem has several numerical advantages. First, note that the least-squares problem has the following matrix algebraic formulation:

$$D \begin{bmatrix} \tilde{A}^\top \\ \tilde{H}^\top \end{bmatrix} = \dot{\tilde{S}}^\top, \quad (20)$$

where the least-squares data matrix $D \in \mathbb{R}^{r \times (r+r^2)}$ and right-hand side $\dot{\tilde{S}} \in \mathbb{R}^{r \times K}$ are given by

$$D = \begin{bmatrix} (\tilde{s}^{(1)})^\top & (\tilde{s}^{(1)} \otimes \tilde{s}^{(1)})^\top \\ (\tilde{s}^{(2)})^\top & (\tilde{s}^{(2)} \otimes \tilde{s}^{(2)})^\top \\ \vdots & \vdots \\ (\tilde{s}^{(K)})^\top & (\tilde{s}^{(K)} \otimes \tilde{s}^{(K)})^\top \end{bmatrix}, \quad \dot{\tilde{S}}^\top = \begin{bmatrix} (\dot{\tilde{s}}^{(1)})^\top \\ (\dot{\tilde{s}}^{(2)})^\top \\ \vdots \\ (\dot{\tilde{s}}^{(K)})^\top \end{bmatrix}. \quad (21)$$

Note that eq. (20) in fact defines r independent least-squares problems, one for each row of the inferred operators \tilde{A} and \tilde{H} . The rows of the inferred operators are independently fit to the r columns of $\dot{\tilde{S}}^\top$, containing data for the evolution of each of the r components of the reduced state \tilde{s} . Equation (20) can be scalably solved for all r right-hand sides by standard linear algebra routines, and additionally, standard QR methods inherently find the norm-minimizing least-squares solution which defines a symmetric quadratic operator \tilde{H} .

Second, since the norm-minimizing solution to eq. (20) satisfies $\tilde{h}_{l,ij} = \tilde{h}_{l,ji}$, each of the r independent least-squares problems defined by eq. (20) has in fact only $r + \binom{r}{2} = r + \frac{r(r+1)}{2}$ degrees of freedom. Thus, the number K of state and time derivative pairs in the data set need only satisfy $K > r + \binom{r}{2}$ for eq. (20) to admit a unique solution with symmetric \tilde{H} (assuming linear independence of the K data pairs). Since r is typically chosen to be small in the context of projection-based model reduction, this data requirement is small relative to the requirements of many black box machine learning methods which assume the availability of ‘big data’. Limiting the data requirements of the method is also our motivation for focusing on the inference of quadratic reduced operators: while the method can in principle be extended to infer matrix operators corresponding to higher-order polynomial terms, the number of degrees of freedom in the least-squares problem grows exponentially as the polynomial order is increased.

Finally, the sensitivity of the linear least-squares problem to perturbations in the data is well-understood and can be ameliorated through standard regularization methods, for example, by adding weights to the Frobenius norm penalty described in eq. (19), as in the Frobenius norm of the reduced operators:

$$\arg \min_{\substack{\tilde{A} \in \mathbb{R}^{r \times r}, \\ \tilde{H} \in \mathbb{R}^{r \times r^2}}} \left(\frac{1}{K} \sum_{k=1}^K \left\| \tilde{A} \tilde{s}^{(k)} + \tilde{H} (\tilde{s}^{(k)} \otimes \tilde{s}^{(k)}) - \dot{\tilde{s}}^{(k)} \right\|_{\mathbb{R}^r}^2 + \gamma_1 \left\| \tilde{A} \right\|_F^2 + \gamma_2 \left\| \tilde{H} \right\|_F^2 \right). \quad (22)$$

This is equivalent to adding a weighted Euclidean norm penalty for each of the r independent least-squares problems whose solutions define rows of \tilde{A} and \tilde{H} , and yields a symmetric operator \tilde{H} as described earlier. However, by increasing the regularization weights, the coefficients in the operators can be driven closer to zero. Explicit regularization also has the effect of making the Operator Inference problem well-posed in the case where even our modest data requirement cannot be met. Operator Inference is therefore especially amenable to the task of learning surrogate models for the high-dimensional simulations that typically arise in scientific settings, where data are often limited due to the expense of the high-dimensional simulations.

4 Lift & Learn for PDEs with non-quadratic nonlinearities

The Operator Inference approach of Section 3, which learns linear and quadratic reduced operators, can be made applicable to PDEs with more general nonlinear terms through the use of lifting variable transformations which expose quadratic structure in the PDE. This section formulates in the PDE setting the *Lift & Learn* method introduced in [46] for ODEs. Section 4.1 motivates our consideration of quadratic structure-exposing transformations. Lifting is defined in Section 4.2, and the Lift & Learn approach is presented in Section 4.3.

4.1 Motivation

While the Operator Inference method fits linear and quadratic reduced operators to data, the method itself makes no assumption of linear or quadratic structure in the governing PDE. Operator Inference can, in principle, be applied to fit a quadratic reduced model to systems governed by PDEs with arbitrary nonlinearities. However, when the Operator Inference parametrization reflects the form of the governing PDE, the Operator Inference model will have the same form as the POD-Galerkin reduced model. This fact is used in [46] to bound in the ODE setting the mean square error of the reduced model over the data by the error due to projection onto the POD subspace. Additionally, the work in [42] uses this fact to show in the ODE setting that Operator Inference non-intrusively recovers the intrusive POD-Galerkin reduced model operators asymptotically, while the work in [41] proves pre-asymptotic recovery guarantees in the ODE setting under certain conditions. Similar analysis applies to the PDE setting considered here [44]. These theoretical analyses motivate our consideration of lifting maps which expose quadratic structure in general nonlinear PDEs.

4.2 Lifting maps

We seek to expose quadratic structure in a general nonlinear PDE through the use of *lifting* maps which transform and/or augment the PDE state with auxiliary variables.

4.2.1 Definition of quadratic lifting

Let $\mathcal{Y} = \mathcal{Y}_1 \times \mathcal{Y}_2 \times \cdots \times \mathcal{Y}_{d'}$ denote a separable Hilbert space with $d' \geq d$, and inner product $\langle \cdot, \cdot \rangle_{\mathcal{Y}}$. Let $\mathcal{T} : \mathcal{X} \rightarrow \mathcal{Y}$ denote a continuous and differentiable nonlinear map. Then, let $w(\cdot, t) = \mathcal{T}(s(\cdot, t))$, and let \mathcal{J} denote the Jacobian of \mathcal{T} .

Definition 1. Consider the nonlinear PDE given by

$$\frac{\partial s}{\partial t} = f(s). \quad (23)$$

The tuple (\mathcal{T}, a, h) is called a quadratic lifting of eq. (23), and the d' -dimensional field $w(x, t)$ is called the lifted state, if w satisfies

$$\frac{\partial w}{\partial t} = \frac{\partial \mathcal{T}(s)}{\partial t} = \mathcal{J}(s) \frac{\partial s}{\partial t} = \mathcal{J}(s) f(s) = a(\mathcal{T}(s)) + h(\mathcal{T}(s)) = a(w) + h(w). \quad (24)$$

The map \mathcal{T} is called the lifting map.

4.2.2 Lifted initial/boundary-value problem

We can use Definition 1 to reformulate the original nonlinear initial/boundary value problem eq. (3). We seek a lifted solution $w : [0, T_{\text{final}}] \rightarrow \mathcal{Y}$ satisfying:

$$\frac{\partial w}{\partial t} = a(w) + h(w), \quad w(0) = \mathcal{T}(s_{\text{init}}). \quad (25)$$

Proposition 1. Suppose the tuple (\mathcal{T}, a, h) is a quadratic lifting as defined in Definition 1. Then, if $s(x, t)$ solves eq. (3), $w(x, t) = \mathcal{T}(s(x, t))$ is a solution of eq. (25).

Proof. It is trivial to verify that if s satisfies the original initial condition, then $\mathcal{T}(s)$ satisfies the lifted initial condition. Then, note that because s satisfies eq. (3), $\frac{\partial}{\partial t} \mathcal{T}(s) = \mathcal{J}(s) f(s)$. By Definition 1, $\mathcal{J}(s) f(s) = a(\mathcal{T}(s)) + h(\mathcal{T}(s))$, so w satisfies eq. (25). \square

4.2.3 An example quadratic lifting

Consider the nonlinear reaction-diffusion equation with cubic reaction term:

$$\frac{\partial s}{\partial t} = f(s) = \frac{\partial^2 s}{\partial x^2} - s^3. \quad (26)$$

Let \mathcal{T} be defined as

$$\mathcal{T} : s \mapsto \begin{pmatrix} s \\ s^2 \end{pmatrix} \equiv \begin{pmatrix} w_1 \\ w_2 \end{pmatrix} = w. \quad (27)$$

Then, the evolution of w satisfies $\frac{\partial w}{\partial t} = a(w) + h(w, w)$, where a and h are defined as

$$a(w) = \begin{pmatrix} \frac{\partial^2 w_1}{\partial x^2} \\ 0 \end{pmatrix}, \quad h(w, w') = \begin{pmatrix} -w_1 w'_2 \\ 2w_1 \frac{\partial^2 w'_1}{\partial x^2} - 2w_2 w'_2 \end{pmatrix}. \quad (28)$$

Proposition 2. The tuple (\mathcal{T}, a, h) given by eqs. (27) and (28) is a quadratic lifting of eq. (26).

Proof. Note that the Jacobian of \mathcal{T} is given by $\mathcal{J}(s) = \begin{pmatrix} 1 \\ 2s \end{pmatrix}$. Thus,

$$\begin{aligned} \frac{\partial w}{\partial t} &= \mathcal{J}(s) f(s) = \begin{pmatrix} 1 \\ 2s \end{pmatrix} \left(\frac{\partial^2 s}{\partial x^2} - s^3 \right) = \begin{pmatrix} \frac{\partial^2 s}{\partial x^2} - s^3 \\ 2s \frac{\partial^2 s}{\partial x^2} - 2s^4 \end{pmatrix} \\ &= \begin{pmatrix} \frac{\partial^2 w_1}{\partial x^2} - w_1 w_2 \\ 2w_1 \frac{\partial^2 w_1}{\partial x^2} - 2(w_2)^2 \end{pmatrix} = a(w) + h(w, w), \end{aligned} \quad (29)$$

for a, h defined in eq. (28), so the tuple (\mathcal{T}, a, h) satisfies Definition 1. \square

4.2.4 Discussion

Lifting maps allow many systems with general nonlinearities to be reformulated with only polynomial nonlinearities, and systems with higher-order polynomial nonlinearities to be reformulated with only quadratic nonlinearities [18]. While there are no universal guarantees of the existence of a lifting, liftings have been derived for many nonlinear PDEs. For example, the lifting of the cubic reaction-diffusion PDE in Section 4.2.3

can be extended to lift reaction-diffusion PDEs with higher-order polynomial source terms to quadratic form with additional auxiliary variables [44]. For fluids problems, both the compressible Euler equations and the Navier-Stokes equations admit a quadratic formulation based on the specific volume representation of the fluid state variables [4, 46]. Quadratic liftings have also been derived for the FitzHugh-Nagumo neuron activation model [27] and the Chafee-Infante equation [6]. In the numerical experiments in Section 5, we will consider a *partial* lifting (in which most—but not all—terms of the lifted PDEs are quadratic in the lifted state) of the PDEs governing a three-dimensional rocket combustion simulation. While we wish to emphasize that the non-intrusive nature of the Operator Inference method allows the flexibility to learn models for PDEs with arbitrary non-quadratic nonlinearities, the identification of even a partial quadratic lifting of the governing PDE can improve the ability of the inferred quadratic operators to model the system dynamics in the lifted variables.

4.3 Lift & Learn for PDEs

Once a lifting map has been identified for a nonlinear PDE, the Lift & Learn approach takes state snapshot $\{s_k\}_{k=1}^K$ and time derivative data $\{\dot{s}_k\}_{k=1}^K$ in the original nonlinear variable representation and applies the lifting map to each snapshot and time derivative:

$$w_k = \mathcal{T}(s_k), \quad \dot{w}_k = \mathcal{J}(s_k)\dot{s}_k, \quad k = 1, 2, \dots, K. \quad (30)$$

The lifted snapshots $\{w_k\}_{k=1}^K$ are used to define a POD basis of rank r in the lifted variables. We then apply the Operator Inference approach of Section 3 to the lifted data to obtain a lifted reduced model.

We emphasize that it is the non-intrusive nature of the Operator Inference method that enables the practical development of reduced models in lifted variables. While our knowledge of the lifted governing equations enables us to write down expressions for the projection-based reduced lifted operators, computing these reduced operators in practice requires numerical evaluation of the $a(\cdot)$ and $h(\cdot, \cdot)$ forms, which are generally not available: even in settings where code for the original governing equations is accessible, code for the lifted operators is generally not available. The Operator Inference approach allows us to learn reduced lifted operators in such practical settings.

5 Numerical examples

We now present numerical experiments from two examples: the first example, presented in Section 5.1, is a one-dimensional heat equation, which demonstrates that choosing an inner product for implementation that is inconsistent with the underlying truth leads to POD basis functions inconsistent with the underlying function space as well as learned operators that are sub-optimal with respect to the underlying function space norm. The second example is a three-dimensional simulation of a model rocket combustor that demonstrates the potential of our learning approach to scale to complex high-dimensional engineering problems. Section 5.2 presents the nonlinear governing equations of the combustion model, and Section 5.3 presents the transformation of the governing equations to approximately quadratic form. In Section 5.4, we introduce the specific test problem we consider and the learning task. Section 5.5 details the reduced model learning formulation. Finally, Section 5.6 presents and discusses the prediction performance of our learned models.

5.1 One-dimensional heat equation

We consider the heat equation,

$$\frac{\partial u}{\partial t} = \frac{\partial^2 u}{\partial x^2}, \quad (31)$$

on the unit spatial domain $x \in (0, 1)$ with homogeneous Dirichlet boundary conditions and random Gaussian initial conditions as described below. The heat equation is discretized using a first-order explicit scheme in time and a second-order central difference scheme in space. The spatial discretization uses a non-uniform mesh: the grid spacing in $(0, 0.3)$ is $\Delta x_1 = 0.05$, the spacing in $(0.3, 0.7)$ is $\Delta x_2 = 0.01$, and the spacing in $(0.7, 1)$ is $\Delta x_3 = 0.1$. This non-uniform spatial discretization was chosen to illustrate the effect of using

different norms (Euclidean vs. $L^2(\Omega)$) in the Operator Inference formulation. Initial conditions $u_0(x)$ are drawn randomly as follows: let $L > 1$ and let $\{\xi_l\}_{l=1}^L$ be independently and identically distributed according to a unit normal distribution. Then, a single random initial condition is given by:

$$u_0(x) = \sqrt{2} \sum_{l=1}^L \xi_l (l\pi)^{-\frac{3}{2}} \sin(l\pi x). \quad (32)$$

Initial conditions drawn randomly according to the above correspond to random draws from the Gaussian random field $\mathcal{N}(0, C_L)$, where C_L is the projection of the covariance kernel $C = \left(\frac{\partial^2}{\partial x^2}\right)^{-\frac{3}{2}}$ onto its L leading principal components. The true principal components of this covariance kernel are the sin functions $\sqrt{2} \sin(l\pi x)$, for $l = 1, 2, \dots, L$. Example initial conditions on our non-uniform mesh are shown in Figure 1.

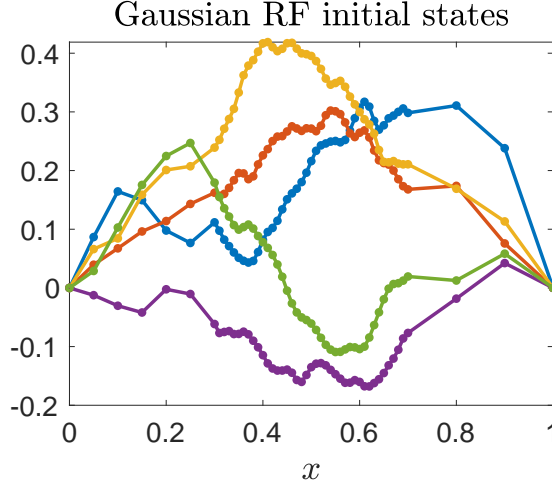


Figure 1: Example initial conditions drawn randomly according to eq. (32). Line markers show non-uniform grid spacing.

We draw 1,000 initial conditions randomly as described with $L = 60$ and evolve the discretized heat equation from $t = 0$ to $t = 0.01$ with time step $\Delta t = 10^{-4}$. The discretized state is saved at every tenth time step. Trajectories from the first 500 initial conditions are used as training data for Operator Inference and the latter 500 trajectories are reserved for testing. We compare results from the function space formulation presented in this work with results from the ODE formulation in earlier works. For the function space formulation, we use a discrete inner product that approximates the $L^2([0, 1])$ inner product using the trapezoidal rule, whereas the ODE formulation uses the Euclidean inner product.

Figure 2 compares the empirical POD modes of the data using the $L^2([0, 1])$ -inner product and the Euclidean inner product with the analytical principal components of the underlying covariance kernel. We note that the use of the $L^2([0, 1])$ -inner product in the function space formulation leads to empirical POD modes that are consistent with the underlying infinite-dimensional truth, whereas the Euclidean inner product used in the ODE setting leads to empirical POD modes that are inconsistent with the underlying distribution.

We use both the function space Operator Inference method and the Euclidean space Operator Inference method to learn reduced models of sizes $r = 1, 2, \dots, 10$ (the original size of the non-uniform mesh is $n = 50$). These learned reduced models are then used to integrate from the reduced initial conditions in time. Figure 3 compares the mean relative $L^2([0, 1])$ -norm errors of the predictions from each learned model. For this heat equation example, there is a clear improvement in prediction accuracy with respect to the underlying function space norm when the function space norm is used in Operator Inference.

Code for this example is available at <https://github.com/elizqian/operator-inference>, which also contains examples of Operator Inference applied to other problems. Demonstration code for the Lift & Learn approach can be found at <https://github.com/elizqian/transform-and-learn>.

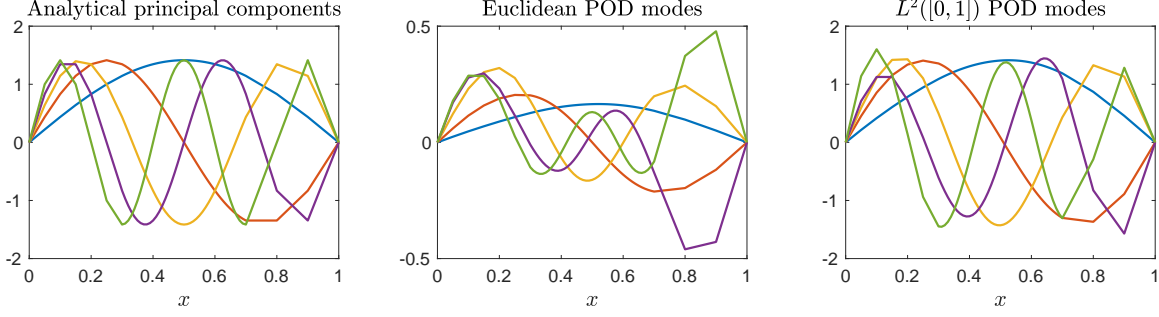


Figure 2: Leading POD basis functions of the heat equation data. Left: analytical principal components. Middle: empirical POD modes in the Euclidean inner product. Right: empirical POD modes in the $L^2([0, 1])$ inner product.

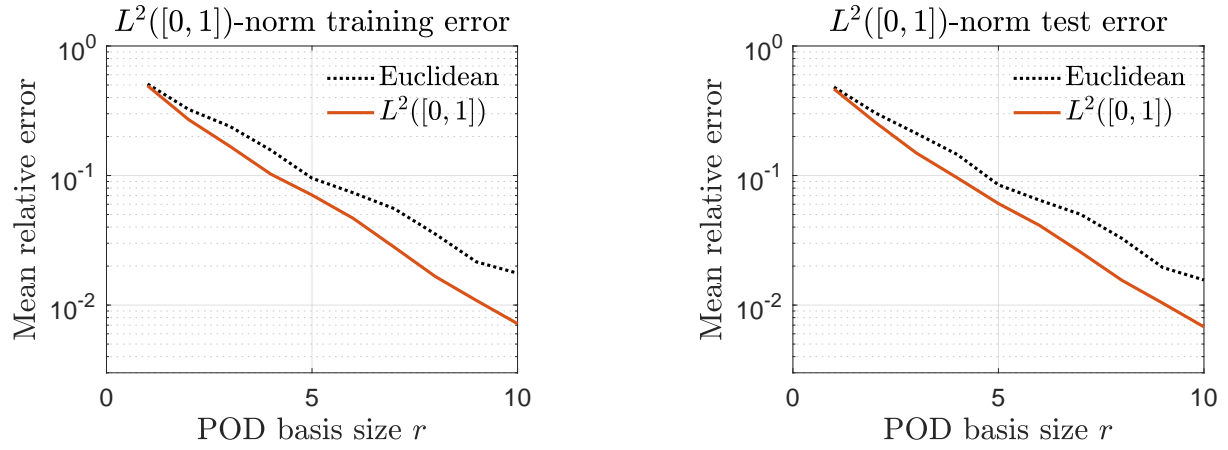


Figure 3: Training and test errors for Operator Inference learned models using function space formulation and Euclidean formulation.

5.2 Combustion problem: original governing PDEs

We now demonstrate the Operator Inference approach on a large-scale problem by learning a reduced model for a three-dimensional simulation of the Continuously Variable Resonance Combustor (CVRC), an experiment at Purdue University that has been extensively studied experimentally and computationally. In particular, several recent works consider learning surrogate models for quasi-one dimensional [55, 45] and two-dimensional [50, 36] versions of its governing equations. The governing PDEs for the CVRC test problem that we consider are the three-dimensional compressible Navier-Stokes equations in conservative form with a flamelet/progress variable chemical model [23, 43]. In this chemical model, the chemistry is parametrized by two variables, the mixture mean, denoted Z_m , and the reaction progress variable, denoted C . Thus, there are $d = 7$ nonlinear state variables:

$$s = (\rho \quad \rho u_1 \quad \rho u_2 \quad \rho u_3 \quad \rho e \quad \rho Z_m \quad \rho C)^\top, \quad (33)$$

where ρ is the density, u_1 , u_2 , and u_3 are the velocities in the three spatial directions, and e is the specific energy. Together, the variables Z_m and C specify a *flamelet manifold* for the chemical species concentrations and reaction source term based on looking up values from a pre-computed table. The governing PDE is given by

$$\frac{\partial s}{\partial t} + \nabla \cdot (F(s) - F_v(s)) = g(s), \quad (34)$$

where $\nabla = \left(\frac{\partial}{\partial x_1} \quad \frac{\partial}{\partial x_2} \quad \frac{\partial}{\partial x_3} \right)^\top$, $F(s)$ is the inviscid flux, given by

$$F(s) = \begin{pmatrix} \rho u_1 \\ \rho u_1^2 + p \\ \rho u_1 u_2 \\ \rho u_1 u_3 \\ \rho u_1 h^0 \\ \rho u_1 Z_m \\ \rho u_1 C \end{pmatrix} \hat{x}_1 + \begin{pmatrix} \rho u_2 \\ \rho u_1 u_2 \\ \rho u_2^2 + p \\ \rho u_2 u_3 \\ \rho u_2 h^0 \\ \rho u_2 Z_m \\ \rho u_2 C \end{pmatrix} \hat{x}_2 + \begin{pmatrix} \rho u_3 \\ \rho u_1 u_3 \\ \rho u_2 u_3 \\ \rho u_3^2 + p \\ \rho u_3 h^0 \\ \rho u_3 Z_m \\ \rho u_3 C \end{pmatrix} \hat{x}_3, \quad (35)$$

$F_v(s)$ is the viscous flux, given by

$$F_v(s) = \begin{pmatrix} 0 \\ \tau_{11} \\ \tau_{21} \\ \tau_{31} \\ \beta_1 \\ \rho D \frac{\partial Z_m}{\partial x_1} \\ \rho D \frac{\partial C}{\partial x_1} \end{pmatrix} \hat{x}_1 + \begin{pmatrix} 0 \\ \tau_{12} \\ \tau_{22} \\ \tau_{32} \\ \beta_2 \\ \rho D \frac{\partial Z_m}{\partial x_2} \\ \rho D \frac{\partial C}{\partial x_2} \end{pmatrix} \hat{x}_2 + \begin{pmatrix} 0 \\ \tau_{13} \\ \tau_{23} \\ \tau_{33} \\ \beta_3 \\ \rho D \frac{\partial Z_m}{\partial x_3} \\ \rho D \frac{\partial C}{\partial x_3} \end{pmatrix} \hat{x}_3, \quad (36)$$

where $\beta_i = \sum_{j=1}^3 u_j \tau_{ji} + \kappa \frac{\partial T}{\partial x_i} - \rho \sum_{l=1}^{n_{\text{sp}}} D \frac{\partial Y_l}{\partial x_i} h_l$, for $i = 1, 2, 3$, and g is the chemical source term, given by $g(s) = (0 \ 0 \ 0 \ 0 \ 0 \ 0 \ \dot{\omega}_C)^\top$. The total enthalpy h^0 satisfies $\rho e = \rho h^0 - p$. The viscous shear stresses are given by $\tau_{ij} = \mu \left(\frac{\partial u_i}{\partial x_j} + \frac{\partial u_j}{\partial x_i} - \frac{2}{3} \frac{\partial u_m}{\partial x_m} \delta_{ij} \right)$, where the three directions are summed over in the term indexed by m .

The temperature T is computed under the ideal gas assumption, $T = \frac{p}{R\rho}$, where $R = \frac{\mathcal{R}}{W_{\text{mol}}}$ is the gas constant, $\mathcal{R} = 8.314 \frac{\text{kJ}}{\text{K} \cdot \text{kmol}}$ is the universal gas constant, and $W_{\text{mol}} = \left(\sum_{l=1}^{n_{\text{sp}}} \frac{Y_l}{W_l} \right)$ is the molecular weight of the species mixture, where Y_l are species mass fractions of the n_{sp} individual chemical species and W_l are their molecular weights. The mass diffusivity D is assumed to be equal to thermal diffusivity α under the unit Lewis number assumption, $D = \alpha = \frac{\kappa}{\rho c_p}$, where κ is the thermal conductivity, and $c_p = \frac{\partial h}{\partial T}$ is the specific heat capacity, defined to be the derivative of the enthalpy h with respect to the temperature T . The enthalpy $h = \sum_l h_l Y_l$ is a convex combination of the species enthalpies, weighted by the species mass fractions, where h_l denotes the enthalpy of the l -th chemical species. The enthalpy of the l -th species has the following dependence on temperature:

$$\frac{h_l(T)}{\mathcal{R}/W_l} = \begin{cases} -\frac{a_{l,1,1}}{T} + a_{l,1,2} \ln T + a_{l,1,3} T + \frac{a_{l,1,4}}{2} T^2 \\ + \frac{a_{l,1,5}}{3} T^3 + \frac{a_{l,1,6}}{4} T^4 + \frac{a_{l,1,7}}{5} T^5 + a_{l,1,8}, & 200\text{K} \leq T \leq 1000\text{K}, \\ -\frac{a_{l,2,1}}{T} + a_{l,2,2} \ln T + a_{l,2,3} T + \frac{a_{l,2,4}}{2} T^2 \\ + \frac{a_{l,2,5}}{3} T^3 + \frac{a_{l,2,6}}{4} T^4 + \frac{a_{l,2,7}}{5} T^5 + a_{l,2,8}, & 1000\text{K} \leq T \leq 6000\text{K}, \end{cases} \quad (37)$$

where the coefficients $a_{l,i,j}$ are given for each species l . The species mass fractions are a function of the flamelet variables, $Y_l = Y_l(Z_m, C)$, where the exact relationship is defined by interpolating between values in a pre-computed table. The source term for the progress variable equation is also defined by a pre-computed table based on the flamelet variables, $\dot{\omega}_C = \dot{\omega}_C(Z_m, C)$.

Previous work on reduced modeling for a different, two-dimensional model of the CVRC has shown that reduced models in the conservative state variables can suffer from a lack of robustness and stability [22]. In order to apply the Lift & Learn formulation of Section 4 to this problem, we seek a partially lifted state variable representation, which we describe in the next section.

5.3 Combustion problem: lifted governing PDEs

Due to the many nonlinearities in the governing equations that are non-quadratic in the conservative state variables, we seek a variable transformation that exposes quadratic structure in these nonlinearities in order to learn quadratic reduced operators. For this complex problem, we use a *partial* lifting, i.e., a variable transformation that transforms many—but not all—of the nonlinearities in governing PDEs into quadratic nonlinearities. Inspired by the quadratic representation of the compressible Euler equations in the specific volume variables [46], we transform the flow variables in the CVRC governing equations from their conservative representation to their specific volume representation, and retain the flamelet variables in their conservative form. Additionally, we add the fluid temperature T to the lifted state because it is a key quantity of interest and we wish to model it directly without recourse to look-up tables. Thus, the lifted variable representation with $d' = 8$ is given by

$$w = (\zeta \quad u_1 \quad u_2 \quad u_3 \quad p \quad \rho Z_m \quad \rho C \quad T)^\top, \quad (38)$$

where $\zeta = \frac{1}{\rho}$. When the specific heat capacity c_p is a constant, the governing equations in the lifted variables eq. (38) contain mostly quadratic nonlinear terms. These governing equations are derived in Appendix B and are given by:

$$\frac{\partial \zeta}{\partial t} = -\nabla \zeta \cdot u + \zeta(\nabla \cdot u), \quad (39a)$$

$$\frac{\partial u_1}{\partial t} = -\zeta \frac{\partial p}{\partial x_1} - u \cdot \nabla u_1 + \zeta \left(\frac{\partial \tau_{11}}{\partial x_1} + \frac{\partial \tau_{12}}{\partial x_2} + \frac{\partial \tau_{13}}{\partial x_3} \right), \quad (39b)$$

$$\frac{\partial u_2}{\partial t} = -\zeta \frac{\partial p}{\partial x_2} - u \cdot \nabla u_2 + \zeta \left(\frac{\partial \tau_{21}}{\partial x_1} + \frac{\partial \tau_{22}}{\partial x_2} + \frac{\partial \tau_{23}}{\partial x_3} \right), \quad (39c)$$

$$\frac{\partial u_3}{\partial t} = -\zeta \frac{\partial p}{\partial x_3} - u \cdot \nabla u_3 + \zeta \left(\frac{\partial \tau_{31}}{\partial x_1} + \frac{\partial \tau_{32}}{\partial x_2} + \frac{\partial \tau_{33}}{\partial x_3} \right), \quad (39d)$$

$$\frac{\partial p}{\partial t} = -\gamma p(\nabla \cdot u) - (u \cdot \nabla p) - u_1 \left(\frac{\partial \tau_{11}}{\partial x_1} + \frac{\partial \tau_{12}}{\partial x_2} + \frac{\partial \tau_{13}}{\partial x_3} \right) \dots \quad (39e)$$

$$\begin{aligned} & - u_2 \left(\frac{\partial \tau_{12}}{\partial x_1} + \frac{\partial \tau_{22}}{\partial x_2} + \frac{\partial \tau_{23}}{\partial x_3} \right) - u_3 \left(\frac{\partial \tau_{13}}{\partial x_1} + \frac{\partial \tau_{23}}{\partial x_2} + \frac{\partial \tau_{33}}{\partial x_3} \right) \dots \\ & + \frac{\partial}{\partial x_1} (u_1 \tau_{11} + u_2 \tau_{12} + u_3 \tau_{13}) + \frac{\partial}{\partial x_2} (u_1 \tau_{21} + u_2 \tau_{22} + u_3 \tau_{23}) \dots \\ & + \frac{\partial}{\partial x_3} (u_1 \tau_{31} + u_2 \tau_{32} + u_3 \tau_{33}) + \frac{\partial q_1}{\partial x_1} + \frac{\partial q_2}{\partial x_2} + \frac{\partial q_3}{\partial x_3}, \end{aligned}$$

$$\frac{\partial \rho Z_m}{\partial t} = -\frac{\partial u_1(\rho Z_m)}{\partial x_1} - \frac{\partial u_2(\rho Z_m)}{\partial x_2} - \frac{\partial u_3(\rho Z_m)}{\partial x_3} + \frac{\kappa}{c_p} \nabla^2 Z_m \quad (39f)$$

$$\frac{\partial \rho C}{\partial t} = -\frac{\partial u_1(\rho C)}{\partial x_1} - \frac{\partial u_2(\rho C)}{\partial x_2} - \frac{\partial u_3(\rho C)}{\partial x_3} + \frac{\kappa}{c_p} \nabla^2 C + \dot{\omega}_C \quad (39g)$$

$$\frac{\partial T}{\partial t} = p \frac{\partial \zeta}{\partial t} + \zeta \frac{\partial p}{\partial t}. \quad (39h)$$

Note that eqs. (39a) to (39d) contain only quadratic dependencies in the lifted variables since the stresses τ_{ij} are linear in the velocity components. In eq. (39e), only the last three terms contain non-quadratic linearities, due to the dependence of the heat fluxes on the unmodeled species mass fractions: $q_i = -\frac{\kappa}{R} \frac{\partial p \zeta}{\partial x_i} + \frac{\kappa}{c_p} \sum_{l=1}^{n_{sp}} \frac{\partial Y_l}{\partial x_i}$. In eq. (39f), the first three terms are quadratic in the velocity components and the variable ρZ_m , while we note for the last three terms that the product rule gives $\frac{\partial \rho Z_m}{\partial x} = \rho \frac{\partial Z_m}{\partial x} + Z_m \frac{\partial \rho}{\partial x}$, which gives the following identity for the x -derivative of Z_m (and similar identities for y and z):

$$\frac{\partial Z_m}{\partial x} = \zeta \frac{\partial \rho Z_m}{\partial x} - Z_m \zeta \frac{\partial \rho}{\partial x} = \zeta \frac{\partial \rho Z_m}{\partial x} + \rho Z_m \frac{\partial \zeta}{\partial x}. \quad (40)$$

Since the first spatial derivatives of Z_m are quadratic in the variable ρZ_m and the specific volume ζ , the second spatial derivatives must also be quadratic in these variables (due to linearity of the derivative operator), so

eq. (39f) is quadratic in the lifted variables. A similar argument shows that eq. (39g) is quadratic in the velocity components, ζ , and ρC , except for the reaction source term $\dot{\omega}_C$, which is non-quadratic due its dependence on the flamelet look-up table. Finally, eq. (39h) is approximately cubic in the specific volume variables because $\frac{\partial p}{\partial t}$ and $\frac{\partial \zeta}{\partial t}$ are approximately quadratic in the specific volume variables. Because the dynamics in the lifted variables are not exactly quadratic, we will employ in our numerical experiments a regularization penalty to combat errors due to the misspecification of the learned model.

5.4 CVRC test problem and learning task

The CVRC geometry and operating conditions are described in Section 5.4.1, and the learning task is described in Section 5.4.2.

5.4.1 Geometry and operating conditions

The CVRC geometry for our problem is a truncated segment of the full combustor studied in [20], and we seek to model the dynamics of the truncated domain under the same inlet operating conditions as in that work. The combustor is depicted in Figure 4 and is cylindrically symmetric around the x_1 -axis. The length of the entire combustor is approximately 28 cm in the axial x_1 -direction. The dynamics are driven by forcing in the form of a 10% fluctuation in the back pressure $p_b(t)$ at the combustor outlet at the right boundary of the domain:

$$p_b(t) = p_{b,0} + 0.1 p_{b,0} \sin(2\pi\nu t), \quad (41)$$

where the forcing frequency is $\nu = 2000$ Hz and the baseline back pressure is $p_{b,0} = 1.1$ MPa.

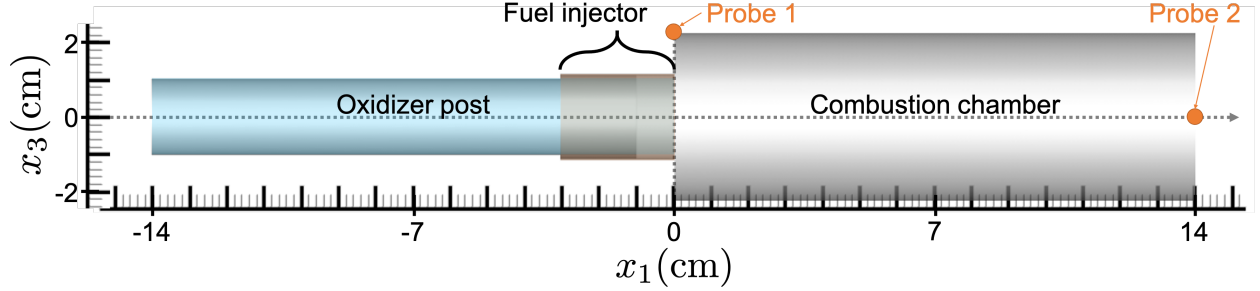


Figure 4: CVRC geometry viewed from negative y -axis and locations of pressure probes. Probe 1 has coordinates $(0, 0, z_{\max})$ and Probe 2 $(x_{\max}, 0, 0)$.

5.4.2 Learning task and available data

Simulation data from solving the original nonlinear equations eq. (34) on a mesh with $n = 2,637,771$ cells is available at 5000 simulation timesteps spaced $\Delta t = 10^{-6}$ seconds apart, corresponding to 5 milliseconds of simulation time between $t = 15$ ms and $t = 20$ ms. Although the conservative formulation eq. (34) is used to discretize the governing equations, yielding

$$n \cdot d = 2,637,771 \cdot 7 = 18,464,397$$

degrees of freedom in the simulation, snapshots are saved for each of the following variables: ρ , u_1 , u_2 , u_3 , p , Z_m , C , T , and enthalpy h . The runtime to compute all 5 milliseconds of simulation time was over 45,000 CPU hours.

The learning task is to use data from the first $K = 3,000$ simulation time steps, from $t = 15$ ms to $t = 17.999$ ms to compute the POD basis and to train a Lift & Learn model. Loading these 3,000 snapshots requires 471 GB of RAM, which makes the processing of this data set memory intensive. For this example, the PDE formulation leads us to use the cell volumes of the simulation to approximate POD basis functions

in the $L^2(\Omega)$ -norm. We will then use the resultant learned model to predict from $t = 15$ ms to $t = 20$ ms: the prediction task is thus to reconstruct the dynamics of the training period *and* to predict dynamics two milliseconds beyond the training period. We will then assess the accuracy of the learned model predictions in pressure, temperature, and the flamelet manifold parameters.

We use the available simulation data to compute the learning variables in eq. (38) for each of the first 3,000 time steps. Because the lifted variables have magnitudes that differ by up to seven orders of the magnitude—pressure has values in MPa ($\mathcal{O}(10^6)$) and ρC and ρZ_m are generally $\mathcal{O}(10^{-1}) - \mathcal{O}(1)$, we center and scale the data in each lifted variable before computing a POD basis. The snapshots in each lifted variable are first centered around the mean field (over the 3,000 training timesteps) in that variable, and then scaled by the maximum absolute value of that variable so that the values for each lifted variable do not exceed the range $[-1, 1]$.

The POD basis is computed in the $L^2(\Omega)$ norm by weighting the discrete norm by the cell volumes of the simulation data. Singular values of the weighted data are shown in the left half of Figure 5. Let η_r denote the relative fraction of energy retained by the r -dimensional POD basis,

$$\eta_r = 1 - \sum_{i=r+1}^{3,000} \sigma_i^2 / \sum_{i=1}^{3,000} \sigma_i^2, \quad (42)$$

where σ_i is the i -th singular value of the data matrix. This retained energy is shown on the right in Figure 5.

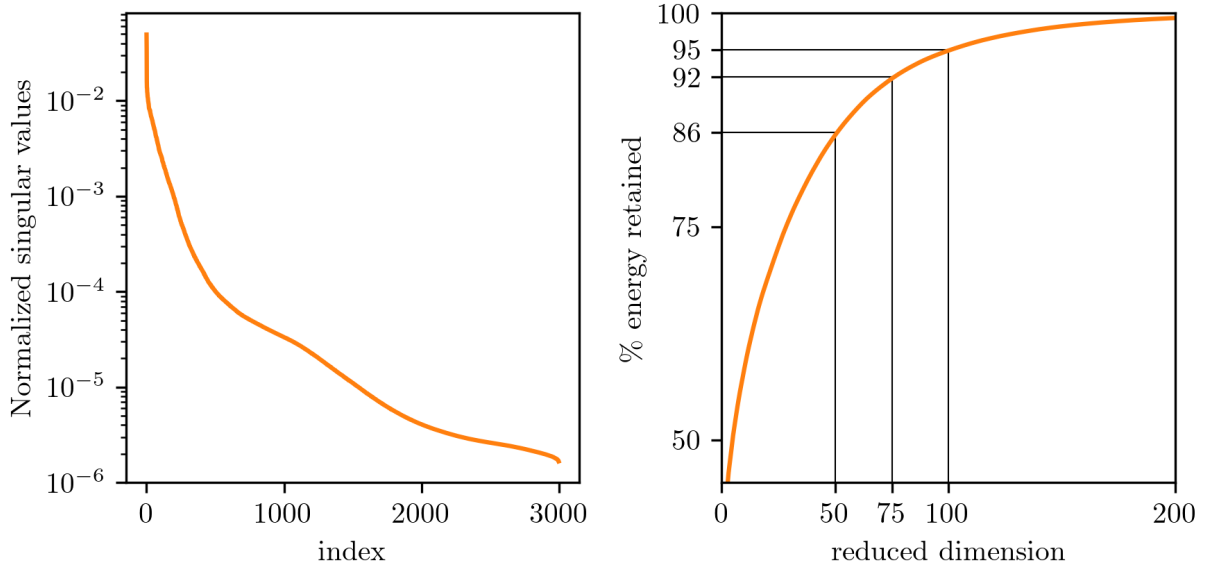


Figure 5: *Left*: Singular values of scaled and centered lifted data, normalized by the sum of all singular values. *Right*: Energy retained by POD bases for the lifted CVRC data.

Figure 5 highlights the retained energy at $r = 50$, $r = 75$, and $r = 100$, which are the basis sizes for which we will fit a reduced model: we discuss the choice of these basis sizes in Section 5.5.2. Due to the complexity of the dynamics of this transport-dominated reacting flow, the decay of the singular values of the data is relatively slow: even with 100 basis functions, only 95% of the POD energy is retained. This is lower than what is considered ideal for traditional projection-based reduced modeling (usually 99.9% or above). However, for our 3,000 available snapshots, the size of the model that can be uniquely specified by the available data limits the sizes of the models we learn.

5.5 Lift & Learn Operator Inference formulation

We now present the regularized operator inference problem used to learn a reduced model for prediction of the CVRC dynamics. Section 5.5.1 describes the form of the model we learn. Section 5.5.2 describes the regularization strategy employed. For this problem, tuning of the regularization parameters is critical to the performance of the method, leading to similar results when the $L^2(\Omega)$ and Euclidean norms are used. The principal purpose of this example is to demonstrate the scalability of our method, so we present results solely for the $L^2(\Omega)$ -norm approach that is the focus of this work.

5.5.1 Parametrization of the learned model

Because most of the terms of the governing equations in the learning variables are linear or quadratic in the learning variables, constant, or linear in the forcing, we will prescribe the following model form for the reduced model to be learned:

$$\frac{\partial \tilde{w}}{\partial t} = \tilde{A}\tilde{w} + \tilde{H}(\tilde{w} \otimes \tilde{w}) + \tilde{G} + \tilde{B}p_\nu(t), \quad (43)$$

where the reduced lifted state \tilde{w} has dimension r , and the reduced operator dimensions are given by $\tilde{A} \in \mathbb{R}^{r \times r}$, $\tilde{H} \in \mathbb{R}^{r \times r^2}$, $\tilde{G} \in \mathbb{R}^r$, and $\tilde{B} \in \mathbb{R}^r$, and the input is defined by $p_\nu(t) = p_b(t) - p_{b,0}$.

5.5.2 Regularized operator inference minimization

As discussed in Section 5.3, the true governing equations in the learning variables contain non-quadratic terms that are not reflected in eq. (43). To reduce the tendency to overfit to the unmodeled dynamics, we regularize the Operator Inference problem as follows:

$$\arg \min_{\tilde{A}, \tilde{H}, \tilde{B}, \tilde{G}} \left(\frac{1}{K} \sum_{k=1}^K \left\| \tilde{A}\tilde{w}_k + \tilde{H}(\tilde{w}_k \otimes \tilde{w}_k) + \tilde{G} + \tilde{B}p_\nu(t_k) - \dot{\tilde{w}}_k \right\|_2^2 \cdots \right. \\ \left. + \gamma_1 \left(\|\tilde{A}\|_F^2 + \|\tilde{B}\|_F^2 + \|\tilde{G}\|_F^2 \right) + \gamma_2 \|\tilde{H}\|_F^2 \right), \quad (44)$$

where γ_1 is the weighting of the regularization penalty on the linear, constant, and input operators, and γ_2 is the regularization penalty on the quadratic operator. We weight the quadratic operator separately because the quadratic terms have a different scaling than the linear terms. The regularization weights γ_1 and γ_2 are tuned using a procedure that minimizes the model prediction error over the training period subject to a growth constraint (see Appendix A for additional information) [36].

Note that even after adding regularization to the minimization in eq. (44), the minimization still decomposes into r independent least-squares problems, one for each row of the reduced operators. Once the structural redundancy of the Kronecker product $\tilde{w} \otimes \tilde{w}$ is accounted for, each of these r independent least-squares problems has $r + \frac{r(r+1)}{2} + 2$ degrees of freedom. The number of degrees of freedom of each of the independent least-squares problems for each of the model sizes we learn, and the regularization weights chosen by our tuning procedure, are tabulated in Table 1.

Model size r	operator inference degrees of freedom	γ_1	γ_2
50	1327	6.95e4	1.62e12
75	2927	3.36e4	3.79e11
100	5152	2.07e2	1.83e11

Table 1: Operator inference specifications for CVRC numerical experiments. The number of degrees of freedom in operator inference is the size of each of the r independent least-squares problems, $r + \frac{r(r+1)}{2} + 2$. Note that the available data set can only fully specify up to 3,000 degrees of freedom without regularization. The tabulated γ_1 and γ_2 values are those chosen by the regularization tuning procedure described in Section 5.5.

Table 1 shows that the three model sizes that we learn represent three different regimes of the least squares Operator Inference problem. Recall that we have $K = 3,000$ training snapshots available to us.

The $r = 50$ model with 1,327 degrees of freedom represents the overdetermined regime, where there are many more data than degrees of freedom. The $r = 100$ model with 5,152 degrees of freedom represents the underdetermined regime, where there are many more degrees of freedom than data. Finally, the $r = 75$ model with 2,927 degrees of freedom is the largest model of the form eq. (43) that can be fully specified by the 3,000 data. In our numerical results, we will compare the performance of the three learned models representing these three regimes.

5.6 Lift & Learn model performance

We now examine the prediction performance of the learned reduced models of sizes $r \in \{50, 75, 100\}$ in the key quantities of interest — the pressure, temperature, and flamelet manifold parameters. Section 5.6.1 describes the metrics we use to assess predictions in the quantities of interest and Section 5.6.2 presents and discusses our results.

5.6.1 Performance metrics

The pressure, temperature, and flamelet manifold parameters are the primary quantities of interest, due to the role of pressure in combustion instability, the temperature limits of materials, and the full specification of the chemical model by the flamelet manifold parameters. To evaluate the Lift & Learn pressure predictions, we will measure the predicted pressure at two point probes, whose locations are shown in Figure 4. Because acoustics are global, these pointwise error measures are accurate reflections of the overall error in pressure prediction.

In contrast, the dynamics in the temperature and flamelet manifold parameters are transport-dominated, so pointwise error measures can be misleading. To assess the performance of the learned model in these variables, we instead consider the cross-correlation between the reference predicted field and the field predicted by the learned model at time t . This measure is informed by the use of cross-correlation in particle image velocimetry analysis of fluid flows, where the cross-correlation is used as a measure of similarity between image frames at different times [24]. Here, we will use the cross-correlation between the fields predicted by different models *at the same time* as a measure of the similarity between predictions.

That is, let $\mathbf{T}^{\text{ref}}(t) \in \mathbb{R}^n$ and $\mathbf{T}^{\text{L\&L}}(t) \in \mathbb{R}^n$ denote the reference and learned model discrete temperature predictions, respectively, and define

$$R_T(t) = \frac{\sum_{i=1}^n (\mathbf{T}_i^{\text{ref}}(t) - \mu_{\mathbf{T}}^{\text{ref}}(t))(\mathbf{T}_i^{\text{L\&L}}(t) - \mu_{\mathbf{T}}^{\text{L\&L}}(t))}{\sigma_{\mathbf{T}}^{\text{ref}} \sigma_{\mathbf{T}}^{\text{L\&L}}}, \quad (45)$$

where $\mu_{\mathbf{T}}^{\text{ref}}(t) \in \mathbb{R}$ and $\mu_{\mathbf{T}}^{\text{L\&L}}(t) \in \mathbb{R}$ are the mean values, respectively, and $\sigma_{\mathbf{T}}^{\text{ref}}(t) \in \mathbb{R}$ and $\sigma_{\mathbf{T}}^{\text{L\&L}}(t) \in \mathbb{R}$ are the standard deviations, respectively, of $\mathbf{T}^{\text{ref}}(t) \in \mathbb{R}^n$ and $\mathbf{T}^{\text{L\&L}}(t) \in \mathbb{R}^n$, respectively. This measure $R_T(t)$ is the Pearson correlation coefficient between the reference and learned model predictions of temperature at time t . We define the correlation measures $R_{Z_m}(t)$ and $R_C(t)$ in a similar way. By definition, the correlations $R_*(t)$ take on values in the range $[-1, 1]$, where $R_*(t) = 1$ indicates perfect correlation and $R_*(t) = -1$ perfect anti-correlation, with $R_*(t) = 0$ indicating no correlation.

5.6.2 Results and discussion

The regularized operator inference minimization in eq. (44) is solved for $r = 50$, $r = 75$, and $r = 100$, with the regularization weights given in Table 1. The inferred reduced operators define a model of the form eq. (43). This inferred model is then numerically integrated using a second-order explicit Runge-Kutta time-stepping scheme to predict the combustor dynamics from the initial condition at $t = 15$ ms.

Figures 6 to 9 give an overview of the learned model prediction performance for the primary quantities of interest. Figure 6 shows the pressure measured at the two probes, while Table 2 reports $L^2(\Omega)$ -errors in the predicted pressure fields. Figures 7 to 9 show cross-sections of the temperature, flamelet mixture mean, and reaction progress fields taken at the $x_2 = 0$ plane of the combustor at each millisecond mark. Field reconstruction is done by multiplying the POD basis vectors by their reduced state coefficients and post-processing the reconstructed states to eliminate non-physical values, i.e., temperatures below 0 were set to 0 and flamelet model parameters outside the range $[0, 1]$ were set to the nearest value in the range.

Non-physical predictions are not unusual in projection-based reduced modeling, since the reduced models evolve coefficients of basis functions rather than the physical state variables themselves. Formulations that embed variable range constraints within the Operator Inference framework are a possible direction of future work, following the ideas proposed in [22].

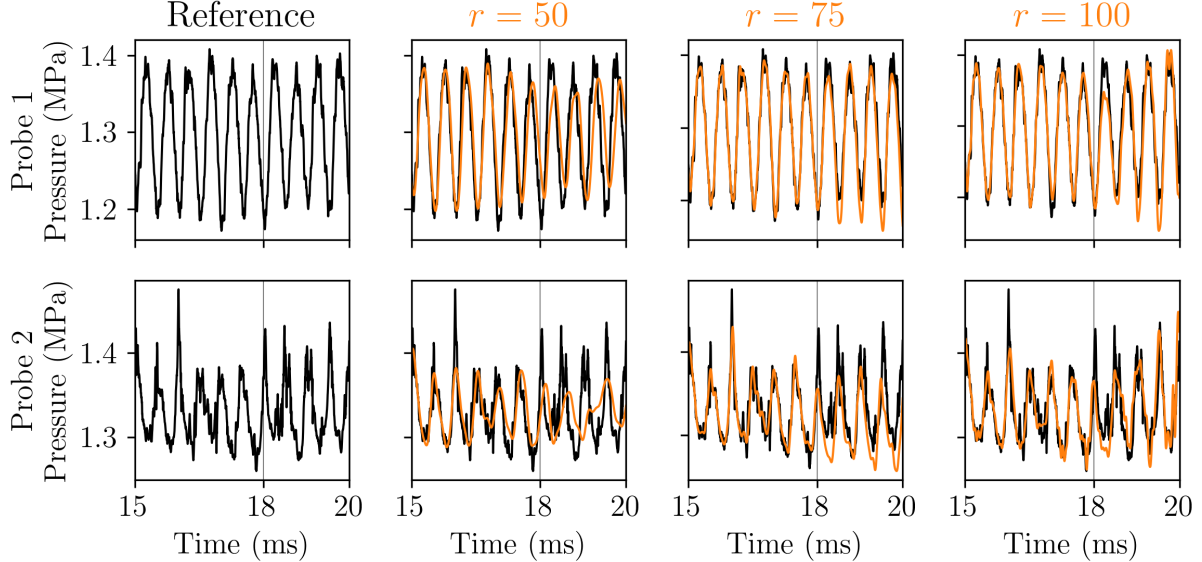


Figure 6: Pressure predictions at probe locations. Probe 1 has coordinates $(0, 0, x_{3,\max})$ and Probe 2 has coordinates $(x_{1,\max}, 0, 0)$. Training period ends at $t = 18$ ms.

Model size r	Pressure error	
	Reconstruction	Prediction
50	0.015	0.032
75	0.007	0.018
100	0.008	0.017

Table 2: Mean relative $L^2(\Omega)$ -errors in pressure predictions of the Operator Inference learned models during the $t \in [15, 18)$ reconstruction period and the $t \in [18, 20]$ prediction period.

The predicted pressure fields of all three learned reduced models demonstrate good agreement with the reference data of the original high-dimensional simulation, with reconstruction errors around 1-2% and generalization errors around 2-3% in the prediction phase (Table 2). In the pressure traces in Figure 6, we observe excellent agreement between the learned reduced models and the original simulation in the dominant frequency and amplitude of the pressure oscillations during the reconstruction phase, with agreement in amplitude deteriorating slightly in the prediction beyond 18ms.

The cross sections of the temperature and combustion parameter fields in Figures 7 to 9 qualitatively illustrate the tradeoff inherent in choosing a basis size r for learned a reduced model. The largest $r = 100$ case is the most expressive, which can be seen by comparing the initial $t = 15$ ms snapshots which simply project the full reference data onto the basis. The $t = 15$ ms snapshots for the $r = 100$ case capture the most structure of the fields, including smaller-scale structures. The $r = 75$ case captures fewer smaller-scale structure and the $r = 50$ case smears out all but the coarser flow features. However, due to the limited available data, the $r = 100$ model cannot be fully specified by the data, and the dynamics of the learned model that results from regularization lead to snapshots at later times that exhibit poorer agreement with the reference simulation (compare for example the $t = 16$ ms temperature snapshots between $r = 100$ and $r = 75$). Another drawback of the underspecified $r = 100$ learning problem is that the resulting model

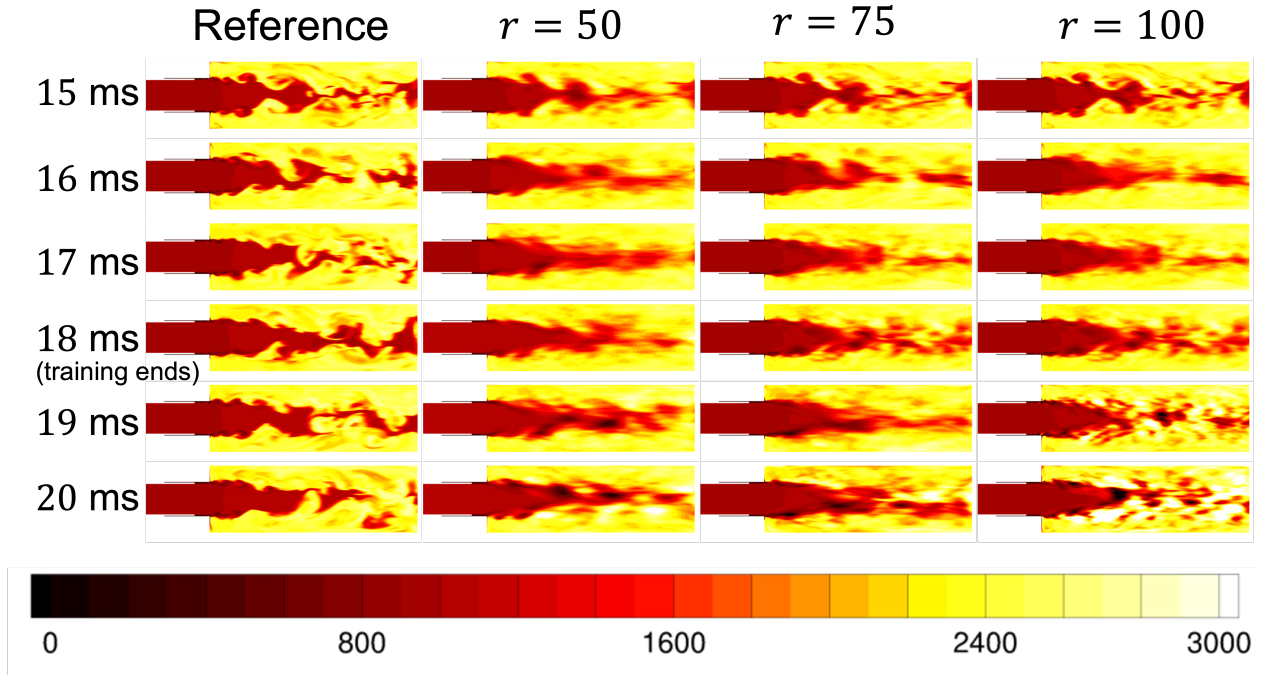


Figure 7: Temperature (Kelvin) field predictions at $x_2 = 0$ plane

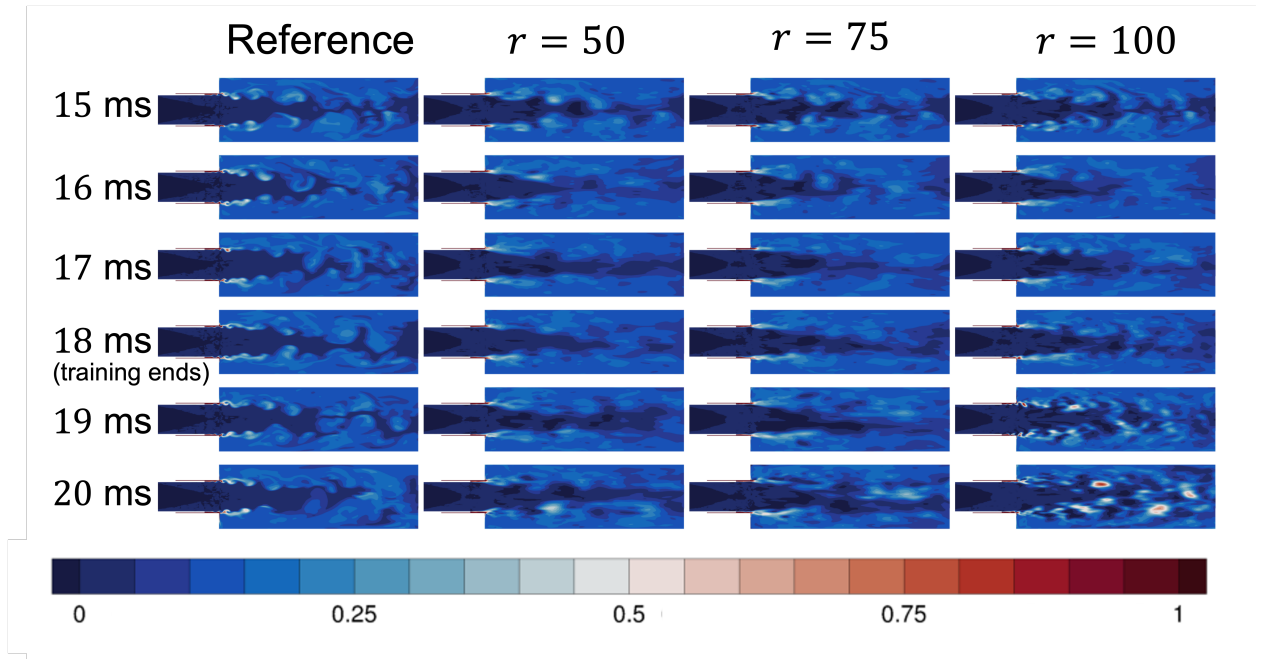


Figure 8: Flamelet mixture mean (Z_m) field predictions at $x_2 = 0$ plane

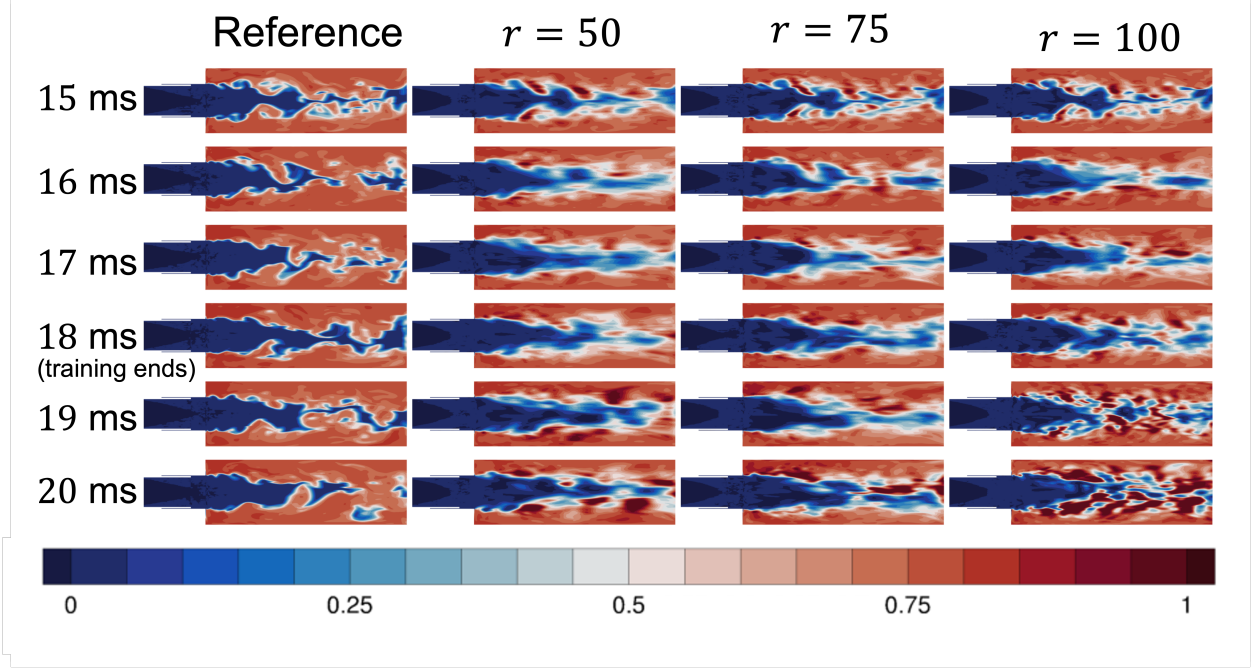


Figure 9: Reaction progress variable (C) field predictions at $x_2 = 0$ plane

predicts several regions where the temperature and flamelet model parameters reach their extremal values, especially at the final $t = 20$ ms (note regions of temperature at 0 K and 3,000 K, well outside the range of the reference). These extreme predictions in the $r = 100$ case illustrate the pitfalls of attempting to fit a model to less data than there are degrees of freedom in the model. While the $r = 50$ and $r = 75$ models exhibit some extreme predictions, these extreme regions are more limited, illustrating the importance of choosing a model size r for which the data allow the learning problem to be fully specified. Building multiple localized Operator Inference reduced models instead of one global reduced model is one way to address this issue, since the dimension of each local reduced model can be kept small [14].

The trade-off between the expressivity of larger r and ability at smaller r to learn accurate dynamics from limited data is illustrated quantitatively in Figure 10, which plots the cross-correlation metric defined in Section 5.6.1 for temperature and the flamelet model parameters. These correlation measures show that while all three learned reduced models yield field predictions that are well-correlated with the reference simulation data during the $t < 18$ ms reconstruction regime, correlation deteriorates sharply for the $t > 18$ ms prediction phase for the larger two model sizes, $r = 75$ and $r = 100$. This quantitative measure illustrates clearly that the $r = 50$ model achieves the best generalization performance in the sense that its reconstruction and prediction correlations are similar, avoiding the sharp decline at the transition to prediction of the other models. The poorer generalization performance of the larger two models is likely the result of the both limited data and model misspecification – as described in Section 5.5.1, the lifted governing equations of the CVRC contain mostly linear and quadratic terms that are reflected in the form of the reduced model, but not all terms have this form. The Operator Inference learning problem for $r = \{75, 100\}$ may be more sensitive to non-quadratic dynamics reflected in the data, leading to poor generalization performance. In contrast, in the $r = 50$ case there is sufficient data to avoid overfitting in the more limited number of degrees of freedom.

Overall, while the learned reduced models fail to capture some aspects of the CVRC dynamics, including some of the high-frequency pressure oscillations and smaller-scale structures of the flow fields, when there is sufficient data for the model size, the learned model can accurately predict large-scale structures (as measured by correlation coefficients above 0.8) and the dominant amplitude and frequency of the pressure oscillations. Our learned models achieve this prediction ability with a dimension reduction of five orders of magnitude relative to that of the reference simulation. This allows the learned reduced model to simulate 5 milliseconds

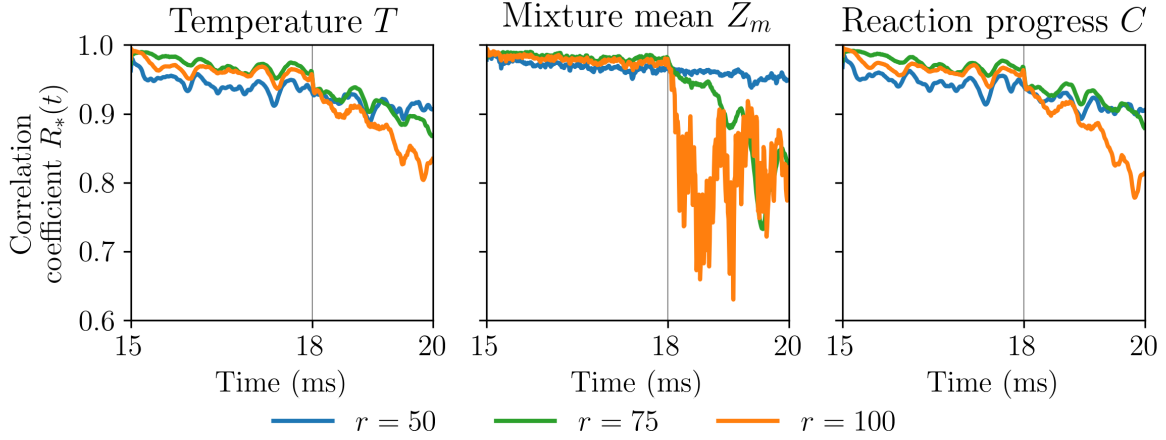


Figure 10: Cross-correlation between learned model prediction and reference data for temperature, flamelet mixture mean, and reaction progress variable. Training data ends at $t = 18$ ms.

of simulation time in a matter of a few seconds of run time, while the high-dimensional simulation that generated the data set required approximately 45,000 CPU hours to generate. This dimension reduction is made possible by our *physics-informed* model learning framework, which transforms the governing equations to mostly-quadratic form, fits a quadratic reduced model, and regularizes against the model’s misspecification of the remaining non-quadratic terms.

6 Conclusions

We have presented Operator Inference for PDEs, a new formulation for scientific machine learning which learns reduced models for systems governed by nonlinear PDEs by parametrizing the model learning problem by low-dimensional polynomial operators which reflect the known polynomial structure of the governing PDE. Operator Inference can be applied to systems governed by more general nonlinear PDEs through Lift & Learn, which uses lifting transformations to expose quadratic structure in the governing PDE. By building this structure due to the governing physics into the learned model representation, our scientific machine learning method reduces the need for massive training data sets when compared to generic representations such as neural networks.

Our Operator Inference formulation generalizes the Operator Inference method previously developed in [42] for systems of ODEs, allowing the learned model parametrization to be determined based solely on the form of the underlying governing physics rather than on the form of the discretization of the PDE. The formulation in the PDE setting learns a mapping between low-dimensional subspaces of the underlying infinite-dimensional Hilbert space, allowing more general variable transformations between Hilbert spaces to be considered, in contrast to [46] which restricts the class of acceptable variable transformations to pointwise transformations. A numerical demonstration for a heat equation problem on a non-uniform grid illustrates that the formulation in the PDE setting yields an algorithm that finds basis functions consistent with the underlying continuous truth and can lead to a lower error than an ODE-based formulation.

We demonstrate the potential of the proposed method to scale to problems of high-dimension by learning reduced operators for a three-dimensional combustion simulation with over 18 million degrees of freedom that requires 45,000 CPU hours to simulate five milliseconds of simulation time. The resulting reduced models accurately predict the amplitude and frequency of pressure oscillations, a key factor in the development of combustion instabilities, with just 50 reduced states, a five order of magnitude dimension reduction. The reduced model can simulate five milliseconds of simulation time in just a few seconds, a speed-up which makes the learned reduced model suitable for use in the many-query computations which support engineering decision making.

Acknowledgments

The authors are grateful for Cheng Huang and Chris Wentland for the data used in the CVRC numerical experiments as well as for several helpful discussions. This work was supported in parts by the National Science Foundation Graduate Research Fellowship Program, the Fannie and John Hertz Foundation, the US Air Force Center of Excellence on Multi-Fidelity Modeling of Rocket Combustor Dynamics award FA9550-17-1-0195, the Air Force Office of Scientific Research MURI program awards FA9550-15-1-0038, FA9550-18-1-0023 and FA9550-21-1-0084, the US Department of Energy Applied Mathematics MMICC Program award DE-SC0019303, and the SUTD-MIT International Design Centre.

A Regularization tuning strategy

To choose the regularization weights γ_1 and γ_2 , we employ a variant of the regularization tuning procedure of [36]. That is, we use the regularization weights that minimize (on a two-dimensional grid) the training error, subject to a constraint that the resultant reduced model have bounded growth within a trial integration period. In more detail, we solve the minimization eq. (44) on a 40×40 grid of values spaced log-uniformly in $(\gamma_1, \gamma_2) \in [10^2, 10^8] \times [10^9, 10^{14}]$. The resultant reduced model is then integrated from $t = 15$ ms to $t = 22$ ms (two milliseconds *beyond* the desired prediction time), and the final regularization parameters are chosen to be the regularization parameters that minimize the error in the predicted reduced coefficients over the training period, subject to the following growth constraint:

$$\max_{\substack{i \leq r \\ k \leq 7000}} |\hat{\mathbf{w}}_i^{\text{trial}}(t_k) - \bar{\mathbf{w}}_i| \leq 1.2 \max_{\substack{i \leq r \\ k \leq 3000}} |\hat{\mathbf{w}}_i^{\text{training}}(t_k) - \bar{\mathbf{w}}_i|, \quad (46)$$

where $\bar{\mathbf{w}}_i$ is the mean of the i -th reduced coefficient over the 3000 training time steps, $\hat{\mathbf{w}}_i^{\text{trial}}(t_k)$ is the value of the i -th reduced coefficient predicted by the inferred model at time t_k , and $\hat{\mathbf{w}}_i^{\text{training}}(t_k)$ is the value of the i -th reduced coefficient in the training data at time t_k . In words, eq. (46) requires that when the reduced model is integrated for the full 7 ms period, no single reduced coefficient deviates more from its training mean more than 20% more than the maximum deviation from the training mean during the training period. We seek models that satisfy this constraint to avoid the selection of regularization parameters that may predict the dynamics of the training period well but become unstable beyond the training period.

We note that all computations in this tuning strategy—the regularized minimization in eq. (44), the integration of the resulting reduced model, and the computation of the error and growth in the reduced coefficients—are dependent only on r -dimensional quantities. This strategy for tuning the regularization parameters is therefore computationally inexpensive. The regularization weights chosen by this tuning strategy for the three model sizes we test are tabulated in Table 1.

B Derivation of lifted CVRC governing PDEs

B.1 Derivation of specific volume equation

Recall that

$$\frac{\partial \rho}{\partial t} = -\nabla \cdot (\rho \mathbf{u}) = -\frac{\partial \rho u_x}{\partial x} - \frac{\partial \rho u_y}{\partial y} - \frac{\partial \rho u_z}{\partial z}. \quad (47)$$

Since $\zeta = \frac{1}{\rho}$, applying the chain rule yields

$$\begin{aligned}
\frac{\partial \zeta}{\partial t} &= \frac{\partial}{\partial t} \frac{1}{\rho} = -\frac{1}{\rho^2} \frac{\partial \rho}{\partial t} = \frac{1}{\rho^2} \left(\frac{\partial \rho u_x}{\partial x} + \frac{\partial \rho u_y}{\partial y} + \frac{\partial \rho u_z}{\partial z} \right) \\
&= \frac{1}{\rho^2} \left(\frac{\partial \rho}{\partial x} u_x + \rho \frac{\partial u_x}{\partial x} + \frac{\partial \rho}{\partial y} u_y + \rho \frac{\partial u_y}{\partial y} + \frac{\partial \rho}{\partial z} u_z + \rho \frac{\partial u_z}{\partial z} \right) \\
&= -\frac{1}{\rho^2} \frac{\partial \rho}{\partial x} (-u_x) - \frac{1}{\rho^2} \frac{\partial \rho}{\partial y} (-u_y) - \frac{1}{\rho^2} \frac{\partial \rho}{\partial z} (-u_z) + \frac{1}{\rho} \left(\frac{\partial u_x}{\partial x} + \frac{\partial u_y}{\partial y} + \frac{\partial u_z}{\partial z} \right) \\
&= -\frac{\partial \zeta}{\partial x} u_x - \frac{\partial \zeta}{\partial y} u_y - \frac{\partial \zeta}{\partial z} u_z + \zeta (\nabla \cdot u) = -\nabla \zeta \cdot u + \zeta (\nabla \cdot u).
\end{aligned} \tag{48}$$

B.2 Derivation of velocity equations

We derive the equation for the evolution of the x -velocity u_x from the equations for the x -momentum ρu_x and for the density:

$$\begin{aligned}
\frac{\partial u_x}{\partial t} &= \frac{1}{\rho} \left(\frac{\partial \rho u_x}{\partial t} - \frac{\partial \rho}{\partial t} u_x \right) \\
&= \frac{1}{\rho} \left(-\frac{\partial \rho u_x^2}{\partial x} + p - \frac{\partial \rho u_x u_y}{\partial y} - \frac{\partial \rho u_x u_z}{\partial z} + \frac{\partial \tau_{xx}}{\partial x} + \frac{\partial \tau_{xy}}{\partial y} + \frac{\partial \tau_{xz}}{\partial z} \dots \right. \\
&\quad \left. + u_x \frac{\partial \rho u_x}{\partial x} + u_x \frac{\partial \rho u_y}{\partial y} + u_x \frac{\partial \rho u_z}{\partial z} \right) \\
&= \frac{1}{\rho} \left(-\frac{\partial p}{\partial x} - u_x^2 \frac{\partial \rho}{\partial x} - \rho \frac{\partial u_x^2}{\partial x} - u_x u_y \frac{\partial \rho}{\partial y} - \rho \frac{\partial u_x u_y}{\partial y} - u_x u_z \frac{\partial \rho}{\partial z} - \rho \frac{\partial u_x u_z}{\partial z} \dots \right. \\
&\quad \left. + u_x^2 \frac{\partial \rho}{\partial x} + \rho u_x \frac{\partial u_x}{\partial x} + u_x u_y \frac{\partial \rho}{\partial y} + \rho u_x \frac{\partial u_y}{\partial y} + u_x u_z \frac{\partial \rho}{\partial z} + \rho u_x \frac{\partial u_z}{\partial z} \dots \right. \\
&\quad \left. + \frac{\partial \tau_{xx}}{\partial x} + \frac{\partial \tau_{xy}}{\partial y} + \frac{\partial \tau_{xz}}{\partial z} \right) \\
&= \frac{1}{\rho} \left(-\frac{\partial p}{\partial x} - \rho \frac{\partial u_x^2}{\partial x} - \rho \frac{\partial u_x u_y}{\partial y} - \rho \frac{\partial u_x u_z}{\partial z} + \rho u_x \left(\frac{\partial u_x}{\partial x} + \frac{\partial u_y}{\partial y} + \frac{\partial u_z}{\partial z} \right) \dots \right. \\
&\quad \left. + \frac{\partial \tau_{xx}}{\partial x} + \frac{\partial \tau_{xy}}{\partial y} + \frac{\partial \tau_{xz}}{\partial z} \right) \\
&= -\zeta \frac{\partial p}{\partial x} - \frac{\partial u_x^2}{\partial x} - \frac{\partial u_x u_y}{\partial y} - \frac{\partial u_x u_z}{\partial z} + u_x \left(\frac{\partial u_x}{\partial x} + \frac{\partial u_y}{\partial y} + \frac{\partial u_z}{\partial z} \right) \dots \\
&\quad + \zeta \left(\frac{\partial \tau_{xx}}{\partial x} + \frac{\partial \tau_{xy}}{\partial y} + \frac{\partial \tau_{xz}}{\partial z} \right) \\
&= -\zeta \frac{\partial p}{\partial x} - 2u_x \frac{\partial u_x}{\partial x} - u_x \frac{\partial u_y}{\partial y} - u_y \frac{\partial u_x}{\partial y} - u_x \frac{\partial u_z}{\partial z} - u_z \frac{\partial u_x}{\partial z} \dots \\
&\quad + u_x \left(\frac{\partial u_x}{\partial x} + \frac{\partial u_y}{\partial y} + \frac{\partial u_z}{\partial z} \right) + \zeta \left(\frac{\partial \tau_{xx}}{\partial x} + \frac{\partial \tau_{xy}}{\partial y} + \frac{\partial \tau_{xz}}{\partial z} \right) \\
&= -\zeta \frac{\partial p}{\partial x} - u_x \frac{\partial u_x}{\partial x} - u_y \frac{\partial u_x}{\partial y} - u_z \frac{\partial u_x}{\partial z} + \zeta \left(\frac{\partial \tau_{xx}}{\partial x} + \frac{\partial \tau_{xy}}{\partial y} + \frac{\partial \tau_{xz}}{\partial z} \right) \\
&= -\zeta \frac{\partial p}{\partial x} - u \cdot \nabla u_x + \zeta \left(\frac{\partial \tau_{xx}}{\partial x} + \frac{\partial \tau_{xy}}{\partial y} + \frac{\partial \tau_{xz}}{\partial z} \right).
\end{aligned} \tag{49}$$

Since the stresses τ_{ij} are linear in the velocities, eq. (49) contains only quadratic terms in the specific volume, pressure, and velocity components. By a similar derivation, we obtain analogous quadratic expressions for

the velocities in the y - and z -directions:

$$\frac{\partial u_y}{\partial t} = -\zeta \frac{\partial p}{\partial y} - u \cdot \nabla u_y + \zeta \left(\frac{\partial \tau_{yx}}{\partial x} + \frac{\partial \tau_{yy}}{\partial y} + \frac{\partial \tau_{yz}}{\partial z} \right), \quad (50)$$

$$\frac{\partial u_z}{\partial t} = -\zeta \frac{\partial p}{\partial z} - u \cdot \nabla u_z + \zeta \left(\frac{\partial \tau_{zx}}{\partial x} + \frac{\partial \tau_{zy}}{\partial y} + \frac{\partial \tau_{zz}}{\partial z} \right). \quad (51)$$

B.3 Derivation of pressure equation

To derive an evolution equation for the pressure p , we use the simplified state equation (which assumes constant c_p):

$$e = c_p T + \frac{1}{2} (u_x^2 + u_y^2 + u_z^2) - \frac{p}{\rho}, \quad (52)$$

or, equivalently, using the relationship $R = \frac{\gamma-1}{\gamma} c_p$ and the ideal gas law,

$$p = (\gamma - 1) \rho e - \frac{\gamma - 1}{2} \rho (u_x^2 + u_y^2 + u_z^2), \quad (53)$$

where γ is the heat capacity ratio (normally a function of T and the species mass fractions Y_l , but assumed constant here). Then,

$$\frac{\partial p}{\partial t} = (\gamma - 1) \left(\frac{\partial \rho e}{\partial t} - \frac{1}{2} \frac{\partial}{\partial t} (\rho (u_x^2 + u_y^2 + u_z^2)) \right) \quad (54)$$

We consider $\frac{\partial \rho e}{\partial t}$ term first, using the simplified state equation to express the energy in terms of the pressure, density, and velocities:

$$\begin{aligned} \frac{\partial \rho e}{\partial t} &= -\frac{\partial}{\partial x} (u_x (\rho e + p)) - \frac{\partial}{\partial y} (u_y (\rho e + p)) - \frac{\partial}{\partial z} (u_z (\rho e + p)) + \mathbf{f}(\tau, j) \\ &= -\frac{\partial}{\partial x} \left(u_x \left(\frac{\gamma}{\gamma-1} p + \frac{1}{2} \rho |u|^2 \right) \right) - \frac{\partial}{\partial y} \left(u_y \left(\frac{\gamma}{\gamma-1} p + \frac{1}{2} \rho |u|^2 \right) \right) \cdots \\ &\quad - \frac{\partial}{\partial z} \left(u_z \left(\frac{\gamma}{\gamma-1} p + \frac{1}{2} \rho |u|^2 \right) \right) + \mathbf{f}(\tau, j) \\ &= -\frac{\gamma}{\gamma-1} \left(\frac{\partial u_x p}{\partial x} + \frac{\partial u_y p}{\partial y} + \frac{\partial u_z p}{\partial z} \right) - \frac{1}{2} \left(\frac{\partial u_x \rho (u_x^2 + u_y^2 + u_z^2)}{\partial x} \cdots \right. \\ &\quad \left. + \frac{\partial u_y \rho (u_x^2 + u_y^2 + u_z^2)}{\partial y} + \frac{\partial u_z \rho (u_x^2 + u_y^2 + u_z^2)}{\partial z} \right) + \mathbf{f}(\tau, j), \end{aligned} \quad (55)$$

where $\mathbf{f}(\tau, j)$ contains the viscous and diffusive heat flux terms, given by:

$$\begin{aligned} \mathbf{f}(\tau, j) &= \frac{\partial}{\partial x} (u_x \tau_{xx} + u_y \tau_{xy} + u_z \tau_{xz}) + \frac{\partial}{\partial y} (u_x \tau_{xy} + u_y \tau_{yy} + u_z \tau_{yz}) \cdots \\ &\quad + \frac{\partial}{\partial z} (u_x \tau_{xz} + u_y \tau_{yz} + u_z \tau_{zz}) + \frac{\partial q_x}{\partial x} + \frac{\partial q_y}{\partial y} + \frac{\partial q_z}{\partial z}. \end{aligned} \quad (56)$$

We now consider the kinetic energy contribution from the x -velocity in eq. (54):

$$\begin{aligned}
\frac{\partial}{\partial t} \left(\frac{1}{2} \rho u_x^2 \right) &= \frac{1}{2} u_x^2 \frac{\partial \rho}{\partial t} + \frac{1}{2} \rho \frac{\partial u_x^2}{\partial t} = \frac{1}{2} u_x^2 \left(-\frac{\partial \rho u_x}{\partial x} - \frac{\partial \rho u_y}{\partial y} - \frac{\partial \rho u_z}{\partial z} \right) + \rho u_x \frac{\partial u_x}{\partial t} \\
&= -\frac{1}{2} u_x^2 \left(\frac{\partial \rho u_x}{\partial x} + \frac{\partial \rho u_y}{\partial y} + \frac{\partial \rho u_z}{\partial z} \right) + \rho u_x \left(-\xi \frac{\partial p}{\partial x} - u_x \frac{\partial u_x}{\partial x} - u_y \frac{\partial u_x}{\partial y} \dots \right. \\
&\quad \left. - u_z \frac{\partial u_x}{\partial z} + \xi \left(\frac{\partial \tau_{xx}}{\partial x} + \frac{\partial \tau_{xy}}{\partial y} + \frac{\partial \tau_{xz}}{\partial z} \right) \right) \\
&= -\frac{1}{2} u_x^2 \left(\frac{\partial \rho u_x}{\partial x} + \frac{\partial \rho u_y}{\partial y} + \frac{\partial \rho u_z}{\partial z} \right) - u_x \frac{\partial p}{\partial x} - u_x \rho u_x \frac{\partial u_x}{\partial x} - u_x \rho u_y \frac{\partial u_x}{\partial y} \dots \\
&\quad - u_x \rho u_z \frac{\partial u_x}{\partial z} + u_x \left(\frac{\partial \tau_{xx}}{\partial x} + \frac{\partial \tau_{xy}}{\partial y} + \frac{\partial \tau_{xz}}{\partial z} \right) \\
&= -\frac{1}{2} u_x^2 \left(\frac{\partial \rho u_x}{\partial x} + \frac{\partial \rho u_y}{\partial y} + \frac{\partial \rho u_z}{\partial z} \right) - u_x \frac{\partial p}{\partial x} - \frac{1}{2} \rho u_x \frac{\partial u_x^2}{\partial x} - \frac{1}{2} \rho u_y \frac{\partial u_x^2}{\partial y} \dots \\
&\quad - \frac{1}{2} \rho u_z \frac{\partial u_x^2}{\partial z} + u_x \left(\frac{\partial \tau_{xx}}{\partial x} + \frac{\partial \tau_{xy}}{\partial y} + \frac{\partial \tau_{xz}}{\partial z} \right) \\
&= -\frac{1}{2} \frac{\partial \rho u_x^3}{\partial x} - \frac{1}{2} \frac{\partial \rho u_y u_x^2}{\partial y} - \frac{1}{2} \frac{\partial \rho u_z u_x^2}{\partial z} - u_x \frac{\partial p}{\partial x} + u_x \left(\frac{\partial \tau_{xx}}{\partial x} + \frac{\partial \tau_{xy}}{\partial y} + \frac{\partial \tau_{xz}}{\partial z} \right). \tag{57}
\end{aligned}$$

We get similar expressions for the $\frac{\partial}{\partial t} \frac{1}{2} \rho u_y^2$ and $\frac{\partial}{\partial t} \frac{1}{2} \rho u_z^2$ terms:

$$\frac{\partial}{\partial t} \frac{1}{2} \rho u_y^2 = -\frac{1}{2} \frac{\partial \rho u_x u_y^2}{\partial x} - \frac{1}{2} \frac{\partial \rho u_y^3}{\partial y} - \frac{1}{2} \frac{\partial \rho u_z u_y^2}{\partial z} - u_y \frac{\partial p}{\partial y} + u_y \left(\frac{\partial \tau_{xy}}{\partial x} + \frac{\partial \tau_{yy}}{\partial y} + \frac{\partial \tau_{yz}}{\partial z} \right), \tag{58}$$

$$\frac{\partial}{\partial t} \frac{1}{2} \rho u_z^2 = -\frac{1}{2} \frac{\partial \rho u_x u_z^2}{\partial x} - \frac{1}{2} \frac{\partial \rho u_y u_z^2}{\partial y} - \frac{1}{2} \frac{\partial \rho u_z^3}{\partial z} - u_z \frac{\partial p}{\partial z} + u_z \left(\frac{\partial \tau_{xz}}{\partial x} + \frac{\partial \tau_{yz}}{\partial y} + \frac{\partial \tau_{zz}}{\partial z} \right). \tag{59}$$

Subtracting eqs. (57) to (59) from eq. (55) we get

$$\begin{aligned}
\frac{\partial \rho e}{\partial t} - \frac{1}{2} \frac{\partial}{\partial t} (\rho (u_x^2 + u_y^2 + u_z^2)) &= -\frac{\gamma}{\gamma-1} \left(\frac{\partial u_x p}{\partial x} + \frac{\partial u_y p}{\partial y} + \frac{\partial u_z p}{\partial z} \right) + u_x \frac{\partial p}{\partial x} + u_y \frac{\partial p}{\partial y} + u_z \frac{\partial p}{\partial z} + \mathfrak{f}(\tau, j) \dots \\
&\quad - u_x \left(\frac{\partial \tau_{xx}}{\partial x} + \frac{\partial \tau_{xy}}{\partial y} + \frac{\partial \tau_{xz}}{\partial z} \right) - u_y \left(\frac{\partial \tau_{xy}}{\partial x} + \frac{\partial \tau_{yy}}{\partial y} + \frac{\partial \tau_{yz}}{\partial z} \right) \dots \\
&\quad - u_z \left(\frac{\partial \tau_{xz}}{\partial x} + \frac{\partial \tau_{yz}}{\partial y} + \frac{\partial \tau_{zz}}{\partial z} \right) \\
&= -\frac{\gamma}{\gamma-1} p \left(\frac{\partial u_x}{\partial x} + \frac{\partial u_y}{\partial y} + \frac{\partial u_z}{\partial z} \right) - \frac{1}{\gamma-1} \left(u_x \frac{\partial p}{\partial x} + u_y \frac{\partial p}{\partial y} + u_z \frac{\partial p}{\partial z} \right) \dots \\
&\quad + \mathfrak{f}(\tau, j) - u_x \left(\frac{\partial \tau_{xx}}{\partial x} + \frac{\partial \tau_{xy}}{\partial y} + \frac{\partial \tau_{xz}}{\partial z} \right) \dots \\
&\quad - u_y \left(\frac{\partial \tau_{xy}}{\partial x} + \frac{\partial \tau_{yy}}{\partial y} + \frac{\partial \tau_{yz}}{\partial z} \right) - u_z \left(\frac{\partial \tau_{xz}}{\partial x} + \frac{\partial \tau_{yz}}{\partial y} + \frac{\partial \tau_{zz}}{\partial z} \right) \\
&= -\frac{\gamma}{\gamma-1} p (\nabla \cdot \mathbf{u}) - \frac{1}{\gamma-1} \mathbf{u} \cdot \nabla p + \mathfrak{f}(\tau, j) - u_x \left(\frac{\partial \tau_{xx}}{\partial x} + \frac{\partial \tau_{xy}}{\partial y} + \frac{\partial \tau_{xz}}{\partial z} \right) \dots \\
&\quad - u_y \left(\frac{\partial \tau_{xy}}{\partial x} + \frac{\partial \tau_{yy}}{\partial y} + \frac{\partial \tau_{yz}}{\partial z} \right) - u_z \left(\frac{\partial \tau_{xz}}{\partial x} + \frac{\partial \tau_{yz}}{\partial y} + \frac{\partial \tau_{zz}}{\partial z} \right). \tag{60}
\end{aligned}$$

This gives the following expression for $\frac{\partial p}{\partial t}$:

$$\begin{aligned}
\frac{\partial p}{\partial t} = & -\gamma p(\nabla \cdot u) - (u \cdot \nabla p) - u_x \left(\frac{\partial \tau_{xx}}{\partial x} + \frac{\partial \tau_{xy}}{\partial y} + \frac{\partial \tau_{xz}}{\partial z} \right) \dots \\
& - u_y \left(\frac{\partial \tau_{xy}}{\partial x} + \frac{\partial \tau_{yy}}{\partial y} + \frac{\partial \tau_{yz}}{\partial z} \right) - u_z \left(\frac{\partial \tau_{xz}}{\partial x} + \frac{\partial \tau_{yz}}{\partial y} + \frac{\partial \tau_{zz}}{\partial z} \right) \dots \\
& + \frac{\partial}{\partial x} (u_x \tau_{xx} + u_y \tau_{xy} + u_z \tau_{xz}) + \frac{\partial}{\partial y} (u_x \tau_{yx} + u_y \tau_{yy} + u_z \tau_{yz}) \dots \\
& + \frac{\partial}{\partial z} (u_x \tau_{zx} + u_y \tau_{zy} + u_z \tau_{zz}) + \frac{\partial q_x}{\partial x} + \frac{\partial q_y}{\partial y} + \frac{\partial q_z}{\partial z}.
\end{aligned} \tag{61}$$

Most of the terms of eq. (61) are quadratic in p and the velocity components. The exception are the diffusive heat flux terms $\frac{\partial q_x}{\partial x}$, $\frac{\partial q_y}{\partial y}$, and $\frac{\partial q_z}{\partial z}$. Under the constant c_p assumption, these terms are simplified from their original definition:

$$\begin{aligned}
q_x &= -\frac{\kappa}{R} \frac{\partial p \zeta}{\partial x} + \frac{\kappa}{c_p} \sum_{l=1}^{n_{\text{sp}}} \frac{\partial Y_l}{\partial x}, \\
q_y &= -\frac{\kappa}{R} \frac{\partial p \zeta}{\partial y} + \frac{\kappa}{c_p} \sum_{l=1}^{n_{\text{sp}}} \frac{\partial Y_l}{\partial y}, \\
q_z &= -\frac{\kappa}{R} \frac{\partial p \zeta}{\partial z} + \frac{\kappa}{c_p} \sum_{l=1}^{n_{\text{sp}}} \frac{\partial Y_l}{\partial z}
\end{aligned} \tag{62}$$

which makes eq. (61) quadratic in p , ζ , u_x , u_y , u_z , and the species variables. Since the species variables are not directly modeled as part of the lifted state, these heat flux terms are not quadratic in the lifted state.

B.4 Derivation of ρZ_m equation

The evolution of the variable ρZ_m is given by the conservative representation as

$$\begin{aligned}
\frac{\partial \rho Z_m}{\partial t} = & -\frac{\partial \rho u_x Z_m}{\partial x} - \frac{\partial \rho u_y Z_m}{\partial y} - \frac{\partial \rho u_z Z_m}{\partial z} + \frac{\partial}{\partial x} \left(\rho D \frac{\partial Z_m}{\partial x} \right) \dots \\
& + \frac{\partial}{\partial y} \left(\rho D \frac{\partial Z_m}{\partial y} \right) + \frac{\partial}{\partial z} \left(\rho D \frac{\partial Z_m}{\partial z} \right).
\end{aligned} \tag{63}$$

Note that $\rho D = \rho \alpha = \frac{\kappa}{c_p}$ (under our unit Lewis number assumption), so under the constant c_p assumption, eq. (63) becomes

$$\frac{\partial \rho Z_m}{\partial t} = -\frac{\partial u_x (\rho Z_m)}{\partial x} - \frac{\partial u_y (\rho Z_m)}{\partial y} - \frac{\partial u_z (\rho Z_m)}{\partial z} + \frac{\kappa}{c_p} \left(\frac{\partial^2 Z_m}{\partial x^2} + \frac{\partial^2 Z_m}{\partial y^2} + \frac{\partial^2 Z_m}{\partial z^2} \right). \tag{64}$$

The first three terms are quadratic in the velocity components and the variable ρZ_m . For the last three terms, note that the product rule gives $\frac{\partial \rho Z_m}{\partial x} = \rho \frac{\partial Z_m}{\partial x} + Z_m \frac{\partial \rho}{\partial x}$, which gives the following identity for the x -derivative of Z_m (and similar identities exist for y and z):

$$\frac{\partial Z_m}{\partial x} = \zeta \frac{\partial \rho Z_m}{\partial x} - Z_m \zeta \frac{\partial \rho}{\partial x} = \zeta \frac{\partial \rho Z_m}{\partial x} + \rho Z_m \frac{\partial \zeta}{\partial x}. \tag{65}$$

Since the first spatial derivatives of Z_m are quadratic in the variable ρZ_m and the specific volume ζ , the second spatial derivatives must also be quadratic in these variables, since the derivative operator is linear.

B.5 Derivation of ρC equation

The derivation of the ρC -evolution equation under the assumption of constant c_p is analogous to that of the ρZ_m -equation. The evolution equation in the conservative representation is given by

$$\begin{aligned} \frac{\partial \rho C}{\partial t} = & -\frac{\partial \rho u_x C}{\partial x} - \frac{\partial \rho u_y C}{\partial y} - \frac{\partial \rho u_z C}{\partial z} + \frac{\partial}{\partial x} \left(\rho D \frac{\partial C}{\partial x} \right) \dots \\ & + \frac{\partial}{\partial y} \left(\rho D \frac{\partial C}{\partial y} \right) + \frac{\partial}{\partial z} \left(\rho D \frac{\partial C}{\partial z} \right) + \dot{\omega}_C. \end{aligned} \quad (66)$$

As in the derivation of eq. (64), we group the variable ρC together in the first three terms and we use the fact that $\rho D = \frac{\kappa}{c_p}$ is a constant to arrive at

$$\frac{\partial \rho C}{\partial t} = -\frac{\partial u_x(\rho C)}{\partial x} - \frac{\partial u_y(\rho C)}{\partial y} - \frac{\partial u_z(\rho C)}{\partial z} + \frac{\kappa}{c_p} \left(\frac{\partial^2 C}{\partial x^2} + \frac{\partial^2 C}{\partial y^2} + \frac{\partial^2 C}{\partial z^2} \right) + \dot{\omega}_C. \quad (67)$$

We have a similar expression for the spatial derivatives of C as we did for those of Z_m in eq. (65):

$$\frac{\partial C}{\partial x} = \zeta \frac{\partial C}{\partial x} - C \zeta \frac{\partial \rho}{\partial x} = \zeta \frac{\partial \rho C}{\partial x} + \rho C \frac{\partial \zeta}{\partial x}, \quad (68)$$

which is quadratic in ζ and ρC . Thus, eq. (67) is almost fully quadratic in the velocity components, the variable ρC , and ζ , with the sole non-quadratic term being the reaction source term $\dot{\omega}_C$.

References

- [1] A. Anandkumar, Ka. Azizzadenesheli, K. Bhattacharya, N. Kovachki, Z. Li, B. Liu, and A. Stuart. Neural operator: Graph kernel network for partial differential equations. In *ICLR 2020 Workshop on Integration of Deep Neural Models and Differential Equations*, 2020.
- [2] P. Astrid, S. Weiland, K. Willcox, and T. Backx. Missing point estimation in models described by proper orthogonal decomposition. *IEEE Transactions on Automatic Control*, 53(10):2237–2251, 2008.
- [3] C. Audouze, F. De Vuyst, and P. B. Nair. Nonintrusive reduced-order modeling of parametrized time-dependent partial differential equations. *Numer. Methods Partial Differential Eq.*, 29:1587–1628, 2013.
- [4] M. Balajewicz, I. Tezaur, and E. Dowell. Minimal subspace rotation on the Stiefel manifold for stabilization and enhancement of projection-based reduced order models for the compressible Navier–Stokes equations. *Journal of Computational Physics*, 321:224–241, 2016.
- [5] M. Barrault, Y. Maday, N. C. Nguyen, and A. T. Patera. An empirical interpolation method: Application to efficient reduced-basis discretization of partial differential equations. *Comptes Rendus Mathématique*, 339(9):667–672, 2004.
- [6] P. Benner and T. Breiten. Two-sided projection methods for nonlinear model order reduction. *SIAM Journal on Scientific Computing*, 37(2):B239–B260, 2015.
- [7] P. Benner, S. Gugercin, and K. Willcox. A survey of projection-based model reduction methods for parametric dynamical systems. *SIAM Review*, 57(4):483–531, 2015.
- [8] G. Berkooz, P. Holmes, and J. L. Lumley. The proper orthogonal decomposition in the analysis of turbulent flows. *Annual Review of Fluid Mechanics*, 25(1):539–575, 1993.
- [9] Nguyen C., K. Veroy, and A. T. Patera. Certified real-time solution of parametrized partial differential equations. In *Handbook of Materials Modeling*, pages 1529–1564. Springer, 2005.
- [10] K. Carlberg, C. Farhat, J. Cortial, and D. Amsallem. The GNAT method for nonlinear model reduction: Effective implementation and application to computational fluid dynamics and turbulent flows. *Journal of Computational Physics*, 242:623–647, 2013.

- [11] K. Champion, B. Lusch, J. N. Kutz, and S. L. Brunton. Data-driven discovery of coordinates and governing equations. *Proceedings of the National Academy of Sciences*, 116(45):22445–22451, 2019.
- [12] S. Chaturantabut and D. Sorensen. Nonlinear model reduction via discrete empirical interpolation. *SIAM Journal on Scientific Computing*, 32(5):2737–2764, 2010.
- [13] Z. Drmac and S. Gugercin. A new selection operator for the discrete empirical interpolation method—improved a priori error bound and extensions. *SIAM Journal on Scientific Computing*, 38(2):A631–A648, 2016.
- [14] R. Geelen and K. Willcox. Localized non-intrusive reduced-order modeling in the operator inference framework. *Philosophical Transactions of the Royal Society A*, To appear, 2021.
- [15] P. K. Goyal and P. Benner. Algebraic gramians for quadratic-bilinear systems and their application in model order reduction. In *22nd International Symposium on Mathematical Theory of Networks and Systems*, 2016.
- [16] M. A. Grepl, Y. Maday, N. C. Nguyen, and A. T. Patera. Efficient reduced-basis treatment of nonaffine and nonlinear partial differential equations. *ESAIM: Mathematical Modelling and Numerical Analysis*, 41(3):575–605, 2007.
- [17] M. A. Grepl and A. T. Patera. A posteriori error bounds for reduced-basis approximations of parametrized parabolic partial differential equations. *ESAIM: Mathematical Modelling and Numerical Analysis*, 39(1):157–181, 2005.
- [18] C. Gu. QLMOR: A projection-based nonlinear model order reduction approach using quadratic-linear representation of nonlinear systems. *IEEE Transactions on Computer-Aided Design of Integrated Circuits and Systems*, 30(9):1307–1320, 2011.
- [19] B. Haasdonk and M. Ohlberger. Efficient reduced models and a posteriori error estimation for parametrized dynamical systems by offline/online decomposition. *Mathematical and Computer Modelling of Dynamical Systems*, 17(2):145–161, 2011.
- [20] M. E. Harvazinski, C. Huang, V. Sankaran, T. W. Feldman, W. E. Anderson, C. L. Merkle, and D. G. Talley. Coupling between hydrodynamics, acoustics, and heat release in a self-excited unstable combustor. *Physics of Fluids*, 27(4):045102, 2015.
- [21] J. S. Hesthaven, G. Rozza, and B. Stamm. *Certified reduced basis methods for parametrized partial differential equations*. Springer, 2016.
- [22] C. Huang and C. L. Duraisamy, K. and Merkle. Investigations and improvement of robustness of reduced-order models of reacting flow. *AIAA Journal*, 57(12):5377–5389, 2019.
- [23] M. Ihme and H. Pitsch. Prediction of extinction and reignition in nonpremixed turbulent flames using a flamelet/progress variable model: 1. a priori study and presumed PDF closure. *Combustion and Flame*, 155(1-2):70–89, 2008.
- [24] R. D. Keane and R. J. Adrian. Theory of cross-correlation analysis of PIV images. *Applied Scientific Research*, 49(3):191–215, 1992.
- [25] I. G. Kevrekidis, C. W. Rowley, and M. O. Williams. A kernel-based method for data-driven Koopman spectral analysis. *Journal of Computational Dynamics*, 2(2):247–265, 2016.
- [26] B. O. Koopman and J. Neumann. Dynamical systems of continuous spectra. *Proceedings of the National Academy of Sciences*, 18(3):255, 1932.
- [27] B. Kramer and K. Willcox. Nonlinear model order reduction via lifting transformations and proper orthogonal decomposition. *AIAA Journal*, 57(6):2297–2307, 2019.

- [28] B. Kramer and K. Willcox. Balanced truncation model reduction for lifted nonlinear systems. *To appear, Realization and Model Reduction of Dynamical Systems*, 2020. arXiv:1907.12084.
- [29] J Nathan Kutz, Steven L Brunton, Bingni W Brunton, and Joshua L Proctor. *Dynamic mode decomposition: data-driven modeling of complex systems*. SIAM, 2016.
- [30] Q. Li, F. Dietrich, E. M. Bollt, and I. G. Kevrekidis. Extended dynamic mode decomposition with dictionary learning: A data-driven adaptive spectral decomposition of the Koopman operator. *Chaos: An Interdisciplinary Journal of Nonlinear Science*, 27(10):103111, 2017.
- [31] Z. Li, N. B. Kovachki, K. Azizzadenesheli, B. Liu, K. Bhattacharya, A. Stuart, and A. Anandkumar. Fourier neural operator for parametric partial differential equations. In *International Conference on Learning Representations*, 2020.
- [32] J.-C. Loiseau and S.L. Brunton. Constrained sparse Galerkin regression. *Journal of Fluid Mechanics*, 838:42–67, 2018.
- [33] L. Lu, P. Jin, G. Pang, Z. Zhang, and G. E. Karniadakis. Learning nonlinear operators via DeepONet based on the universal approximation theorem of operators. *Nature Machine Intelligence*, 3(3):218–229, 2021.
- [34] J. L. Lumley. The structure of inhomogeneous turbulent flows. *Atmospheric Turbulence and Radio Wave Propagation*, 1967.
- [35] L. Mainini and K. E. Willcox. Data to decisions: Real-time structural assessment from sparse measurements affected by uncertainty. *Computers & Structures*, 182:296–312, 2017.
- [36] Shane A McQuarrie, Cheng Huang, and Karen E Willcox. Data-driven reduced-order models via regularised operator inference for a single-injector combustion process. *Journal of the Royal Society of New Zealand*, 51(2):194–211, 2021.
- [37] I. Mezić. Analysis of fluid flows via spectral properties of the Koopman operator. *Annual Review of Fluid Mechanics*, 45:357–378, 2013.
- [38] Igor Mezić. Spectral properties of dynamical systems, model reduction and decompositions. *Nonlinear Dynamics*, 41(1):309–325, 2005.
- [39] N. H. Nelsen and A. M. Stuart. The random feature model for input-output maps between Banach spaces. *SIAM Journal on Scientific Computing*, to appear, 2021.
- [40] N.C. Nguyen, A.T. Patera, and J. Peraire. A best points interpolation method for efficient approximation of parametrized functions. *International Journal for Numerical Methods in Engineering*, 73(4):521–543, 2008.
- [41] B. Peherstorfer. Sampling low-dimensional Markovian dynamics for pre-asymptotically recovering reduced models from data with operator inference. *SIAM Journal on Scientific Computing*, To appear, 2021.
- [42] B. Peherstorfer and K. Willcox. Data-driven operator inference for nonintrusive projection-based model reduction. *Computer Methods in Applied Mechanics and Engineering*, 306:196–215, 2016.
- [43] C. D. Pierce. *Progress-variable approach for large-eddy simulation of turbulent combustion*. PhD thesis, Stanford University, 2001.
- [44] E. Qian. *A scientific machine learning approach to learning reduced models for nonlinear partial differential equations*. PhD thesis, Massachusetts Institute of Technology, 2 2021.
- [45] E. Qian, B. Kramer, A. N. Marques, and K. Willcox. Transform & Learn: A data-driven approach to nonlinear model reduction. In *AIAA Aviation 2019 Forum*, page 3707, 2019.

- [46] E. Qian, B. Kramer, B. Peherstorfer, and K. Willcox. Lift & learn: Physics-informed machine learning for large-scale nonlinear dynamical systems. *Physica D: Nonlinear Phenomena*, Volume 406, 2020.
- [47] G. Rozza, D. B. P. Huynh, and A. T. Patera. Reduced basis approximation and a posteriori error estimation for affinely parametrized elliptic coercive partial differential equations. *Archives of Computational Methods in Engineering*, 15(3):229–275, 2008.
- [48] P. J. Schmid. Dynamic mode decomposition of numerical and experimental data. *Journal of Fluid Mechanics*, 656:5–28, 2010.
- [49] L. Sirovich. Turbulence and the dynamics of coherent structures. I-coherent structures. *Quarterly of Applied Mathematics*, 45:561–571, 1987.
- [50] R. Swischuk, B. Kramer, C. Huang, and K. Willcox. Learning physics-based reduced-order models for a single-injector combustion process. *AIAA Journal*, 58(6):2658–2672, 2020.
- [51] R. Swischuk, L. Mainini, B. Peherstorfer, and K. Willcox. Projection-based model reduction: Formulations for physics-based machine learning. *Computers and Fluids*, 179:704–717, 2019.
- [52] N. Takeishi, Y. Kawahara, and T. Yairi. Learning Koopman invariant subspaces for dynamic mode decomposition. In *Advances in Neural Information Processing Systems*, pages 1130–1140, 2017.
- [53] K. Veroy and A. T. Patera. Certified real-time solution of the parametrized steady incompressible Navier–Stokes equations: rigorous reduced-basis a posteriori error bounds. *International Journal for Numerical Methods in Fluids*, 47(8-9):773–788, 2005.
- [54] K. Veroy, D. V. Rovas, and A. T. Patera. A posteriori error estimation for reduced-basis approximation of parametrized elliptic coercive partial differential equations: “convex inverse” bound conditioners. *ESAIM: Control, Optimisation and Calculus of Variations*, 8:1007–1028, 2002.
- [55] Q. Wang, J. S. Hesthaven, and D. Ray. Non-intrusive reduced order modeling of unsteady flows using artificial neural networks with application to a combustion problem. *Journal of Computational Physics*, 384:289–307, 2019.
- [56] M. O. Williams, I. G. Kevrekidis, and C. W. Rowley. A data-driven approximation of the Koopman operator: Extending dynamic mode decomposition. *Journal of Nonlinear Science*, 25(6):1307–1346, 2015.